Title

Functional landscape of SARS-CoV-2 cellular restriction

Journal

Molecular Cell, 81(12)

ISSN

1097-2765

Authors

Martin-Sancho, Laura
Lewinski, Mary K
Pache, Lars
et al.

Publication Date

2021-06-01

DOI

10.1016/j.molcel.2021.04.008

Peer reviewed

Molecular Cell

Resource

Functional landscape of SARS-CoV-2 cellular restriction

Graphical abstract

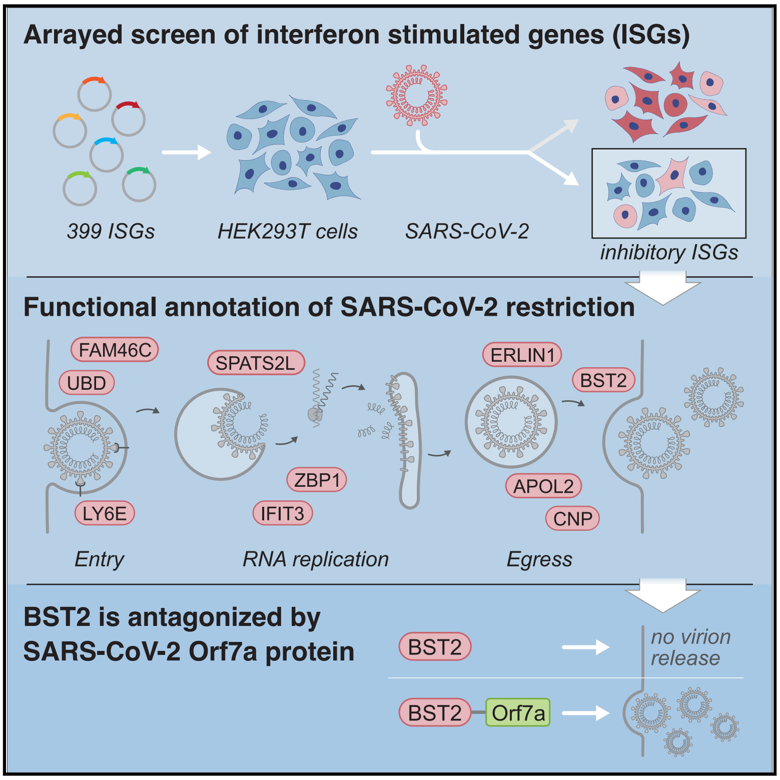

Highlights

- IFN-mediated restriction of SARS-CoV-2 relies on a subset of 65 ISGs
- ER- and Golgi-resident proteins are enriched among the inhibitory ISGs
- BST2 inhibits SARS-CoV-2 release and is antagonized by virally encoded Orf7a
- Eight of the ISGs inhibit SARS-CoV-1 and SARS-CoV-2 but no unrelated viruses

Authors

Laura Martin-Sancho,
Mary K. Lewinski, Lars Pache, ...,
Judd F. Hultquist, John Guatelli,
Sumit K. Chanda

Correspondence

schanda@sbpdiscovery.org

In brief

Deficient interferon responses to SARS-CoV-2 infection have been associated with severe COVID-19. Martin-Sancho et al. utilized a gain-of-function screen to identify interferon-stimulated effectors that govern innate immune responses to SARS-CoV-2. These factors could underlie genetic predisposition to severe COVID-19 and can serve as candidates for development of antiviral therapies.

Martin-Sancho et al., 2021, Molecular Cell *81*, 2656–2668
June 17, 2021 © 2021 Elsevier Inc.
https://doi.org/10.1016/j.molcel.2021.04.008

CellPress

CellPress Molecular Cell

Resource

Functional landscape of SARS-CoV-2 cellular restriction

Laura Martin-Sancho,[1] Mary K. Lewinski,[2] Lars Pache,[1] Charlotte A. Stoneham,[2] Xin Yin,[1] Mark E. Becker,[3] Dexter Pratt,[4] Christopher Churas,[4] Sara B. Rosenthal,[4] Sophie Liu,[4] Stuart Weston,[5] Paul D. De Jesus,[1] Alan M. O'Neill,[6] Anshu P. Gounder,[1] Courtney Nguyen,[1] Yuan Pu,[1] Heather M. Curry,[1] Aaron L. Oom,[2] Lisa Miorin,[7,8] Ariel Rodriguez-Frandsen,[1] Fan Zheng,[4] Chunxiang Wu,[9] Yong Xiong,[9] Matthew Urbanowski,[7] Megan L. Shaw,[7,10] Max W. Chang,[4] Christopher Benner,[4] Thomas J. Hope,[3] Matthew B. Frieman,[5] Adolfo García-Sastre,[7,8,11,12] Trey Ideker,[4,13] Judd F. Hultquist,[14] John Guatelli,[2] and Sumit K. Chanda[1,15,*]

[1]Immunity and Pathogenesis Program, Sanford Burnham Prebys Medical Discovery Institute, La Jolla, CA 92037, USA
[2]Department of Medicine, University of California San Diego, and the VA San Diego Healthcare System, San Diego, CA 92161, USA
[3]Department of Cell and Developmental Biology, Northwestern University Feinberg School of Medicine, Chicago, IL 60611, USA
[4]Department of Medicine, University of California San Diego, La Jolla, CA 92093, USA
[5]Department of Microbiology and Immunology, University of Maryland School of Medicine, Baltimore, MD 21201, USA
[6]Department of Dermatology, University of California San Diego, La Jolla, CA 92093, USA
[7]Department of Microbiology, Icahn School of Medicine at Mount Sinai, New York, NY 10029-5674, USA
[8]Global Health and Emerging Pathogens Institute, Icahn School of Medicine at Mount Sinai, New York, NY 10029-5674, USA
[9]Department of Molecular Biophysics and Biochemistry, Yale University, New Haven, CT 06510, USA
[10]Department of Medical Biosciences, University of the Western Cape, Cape Town 7535, South Africa
[11]Department of Medicine, Division of Infectious Diseases, Icahn School of Medicine at Mount Sinai, New York, NY 10029-5674, USA
[12]The Tisch Institute, Icahn School of Medicine at Mount Sinai, New York, NY 10029-5674, USA
[13]Department of Computer Science and Engineering, University of California San Diego, La Jolla, CA 92093, USA
[14]Division of Infectious Diseases, Northwestern University Feinberg School of Medicine, Chicago, IL 60611, USA
[15]Lead contact
*Correspondence: schanda@sbpdiscovery.org

https://doi.org/10.1016/j.molcel.2021.04.008

SUMMARY

A deficient interferon (IFN) response to severe acute respiratory syndrome coronavirus 2 (SARS-CoV-2) infection has been implicated as a determinant of severe coronavirus disease 2019 (COVID-19). To identify the molecular effectors that govern IFN control of SARS-CoV-2 infection, we conducted a large-scale gain-of-function analysis that evaluated the impact of human IFN-stimulated genes (ISGs) on viral replication. A limited subset of ISGs were found to control viral infection, including endosomal factors inhibiting viral entry, RNA binding proteins suppressing viral RNA synthesis, and a highly enriched cluster of endoplasmic reticulum (ER)/Golgi-resident ISGs inhibiting viral assembly/egress. These included broad-acting antiviral ISGs and eight ISGs that specifically inhibited SARS-CoV-2 and SARS-CoV-1 replication. Among the broad-acting ISGs was BST2/tetherin, which impeded viral release and is antagonized by SARS-CoV-2 Orf7a protein. Overall, these data illuminate a set of ISGs that underlie innate immune control of SARS-CoV-2/SARS-CoV-1 infection, which will facilitate the understanding of host determinants that impact disease severity and offer potential therapeutic strategies for COVID-19.

INTRODUCTION

The ongoing coronavirus disease 2019 (COVID-19) pandemic, caused by severe acute respiratory syndrome coronavirus 2 (SARS-CoV-2), is responsible for a reported 126 million infections and over 2.76 million deaths worldwide as of this writing. Following infection with SARS-CoV-2, COVID-19 clinical presentation ranges from asymptomatic or mild (suggested to account for ~80% of infections) to severe disease that typically requires hospitalization and assisted respiration (Huang et al., 2020). While age and comorbidities, such as obesity and cardiovascular disease, have been linked to COVID-19 severity, recent data suggest that innate immune responses to viral infection are also a critical determinant of disease outcome (Mathew et al., 2020). For instance, loss-of-function mutations in the immune sensor *TLR7* and downregulation of the type I interferon (IFN) response have been associated with severe COVID-19 (van der Made et al., 2020). In addition, two recent studies that conducted an integrated immune analysis of COVID-19 patients found impaired IFN responses in severe

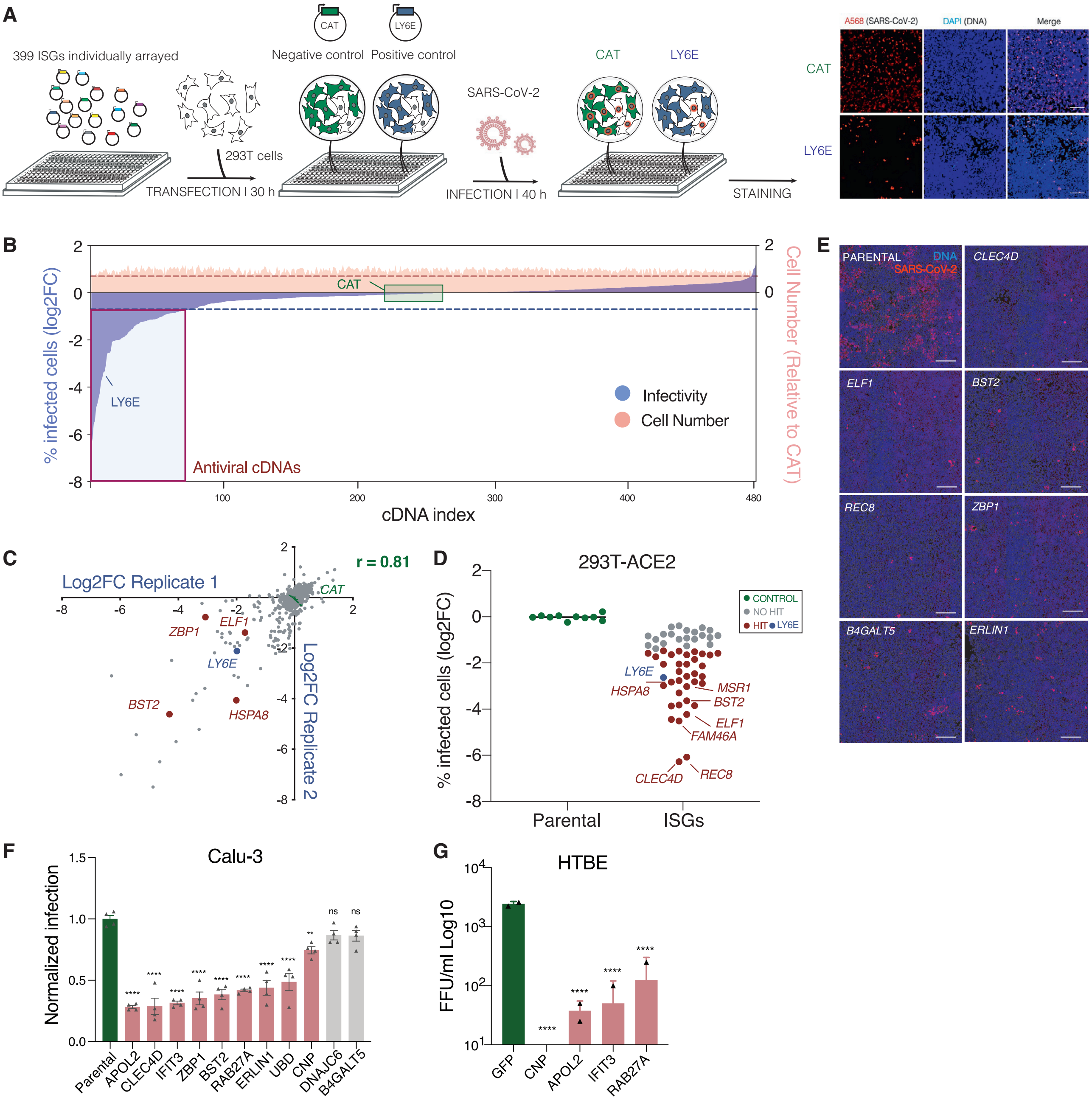

Figure 1. IFN-mediated restriction of SARS-CoV-2 relies on a limited subset of ISGs

(A) Schematic representation of the gain-of-function screen to identify ISGs that inhibit SARS-CoV-2 replication.

(B) Ranked log2FC of the percentage of infected cells (SARS-CoV-2 N$^+$ cells, blue shading) and normalized cell number (pink shading) after individual overexpression of 399 human ISGs and controls. Values are relative to the negative control *CAT*. Dashed lines illustrate cut offs for antiviral ISG hit calling strategy; the dotted blue line indicates log2FC infection = 4 × standard deviations (SDs) log2FC of *CAT* log2FC, and the dotted pink line indicates cell number = 70% of *CAT*. Controls are shown (*CAT*, negative; *LY6E*, positive).

(C) Correlation plots between screens. r, Pearson correlation coefficient.

(D) 293T-ACE2 cells transduced with lentiviruses carrying each of the identified ISGs were infected with SARS-CoV-2 (MOI = 0.25) for 40 h prior to immunostaining for viral SARS-CoV-2 nucleoprotein (N). Data represent mean log2FC values (percentage of N$^+$ cells relative to parental control wells) from three independent experiments (n = 3).

(E) Representative images are shown. Scale bars, 10 μm.

(F) Calu-3 cells transduced with lentiviruses encoding the indicated ISGs were infected with SARS-CoV-2 (MOI =1.5) for 48 h prior to immunostaining for viral N protein. Data show mean ± SEM normalized infection (percentage of infected cells relative to parental control wells) from one representative experiment in quadruplicate (n = 4).

(legend continued on next page)

and critically ill patients (Arunachalam et al., 2020; Hadjadj et al., 2020). Further support for the role of type I IFN in COVID-19 outcome comes from a study of 127 patients receiving IFN beta-1b in combination with lopinavir-ritonavir and ribavirin, which reported lower SARS-CoV-2 viral load and shedding in the lungs and reduced length of hospitalization (Hung et al., 2020). Taken together, these data underscore an emerging role for IFN-mediated cellular responses in the control of SARS-CoV-2 infection and COVID-19 severity.

Viral infection is sensed by pattern recognition receptors (PRRs), which initiate a signaling cascade that produces cytokines, including production of type I and III IFNs. These IFNs promote the transcriptional activation of hundreds of IFN-stimulated genes (ISGs), many of which exert antiviral activities (Schoggins et al., 2011). Concerted expression and regulation of these PRRs and downstream signaling molecules, transcription factors, and effectors are necessary to mount a successful antiviral response. Thus, viruses have developed various strategies to interfere with and evade these antiviral programs (García-Sastre, 2017). Recent work has shown that SARS-CoV-2 infection is sensed by the cytoplasmic sensor MDA5 and induces IFN production (Yin et al., 2021). Accordingly, RNA sequencing (RNA-seq) of COVID-19 patient samples and *in vitro* infection models revealed upregulation of ISGs (Blanco-Melo et al., 2020; Emanuel et al., 2020; Lamers et al., 2020; Overmyer et al., 2020; Sun et al., 2020). In addition, SARS-CoV-2 is sensitive to IFN treatment (Lokugamage et al., 2020) and the activity of several ISGs, including *LY6E*, which inhibited replication of SARS-CoV-2 (Pfaender et al., 2020), and the ISGs *AXIN2*, *CH25H*, *EPSTI1*, *GBP5*, *IFIH1*, *IFITM2*, and *IFITM3*, which were found to block entry of a pseudotyped vesicular stomatitis virus (VSV) harboring SARS-CoV-2 spike (S) protein (Zang et al., 2020). Ultimately, a comprehensive evaluation of ISGs that inhibit infection of SARS-CoV-2 will be necessary to understand the cellular control of viral infection and their potential impact on COVID-19 outcome.

To uncover the cellular antiviral response to SARS-CoV-2 infection, we conducted a gain-of-function screen using 399 human ISGs. These data revealed that restriction of SARS-CoV-2 is mediated by a limited subset of 65 ISGs, mostly endoplasmic reticulum (ER)- and Golgi-resident proteins that are reported regulators of ER-associated protein degradation (ERAD), lipid membrane composition, and vesicle transport (Fitzgerald, 2011; Inoue et al., 2015; Mo et al., 2020). Among the inhibitory ISGs was BST2, which was found to inhibit viral egress and be antagonized by the SARS-CoV-2 accessory protein Orf7a. These factors represent attractive targets for therapeutic intervention and have the potential to provide insight into the host molecular and genetic determinants of early immune regulation that may contribute to COVID-19 outcome.

RESULTS AND DISCUSSION

IFN-mediated restriction of SARS-CoV-2 relies on a limited subset of ISGs

To define the cellular effectors that act to limit SARS-CoV-2 infection, we first sought to determine which genes are activated upon type I IFN stimulation (hereafter referred to as ISGs) in disease-relevant cell types. Human tracheobronchial epithelial (HTBE) and human alveolar epithelial A549 cells were treated with IFN for 8 h and then subjected to RNA-seq. Using cutoff criteria of $\log_2$ fold change (log2FC) > 1.5 and p value < 0.05, we identified 139 ISGs upregulated in HTBE cells, 121 ISGs upregulated in A549 cells, and 152 ISGs upregulated in both HTBE and A549 cells (Figure S1A). This dataset encompassed ISGs with previously characterized broad-acting antiviral activities that included *MX1*, *OAS1*, *OASL*, and *IFI6* (Hubel et al., 2019). In addition, Schoggins et al. previously assembled a list of 387 curated ISGs, of which 149 overlapped with the HTBE/A549 dataset (Figure S1B) (Schoggins et al., 2011). We combined these experimental and published datasets and identified 399 ISGs as available, validated, and full-sequence-length cDNA clones (Figure S1B; Table S1).

Next, we evaluated the ability of these 399 ISGs to inhibit SARS-CoV-2 replication using ectopic expression screening. These studies were conducted using the human epithelial cell line 293T, as these cells can be transfected with high efficiency, support productive replication of SARS-CoV-2 when expressing the viral entry factors *ACE2* and *TMPRSS2* (Hoffmann et al., 2020), and respond to IFN treatment (Figure S1C). 293T cells were transfected with individual ISGs along with *ACE2* and *TMPRSS2* for 30 h and then challenged with SARS-CoV-2 at a low multiplicity of infection (MOI = 0.0625). Cells were fixed at 40 h post-infection, and the percentage of infected cells was determined using immunostaining for SARS-CoV-2 nucleoprotein (N) (Figure 1A). cDNA encoding chloramphenicol acetyltransferase (*CAT*) was included on each plate as negative control, and cDNA encoding the SARS-CoV-2 negative regulator *LY6E* (Pfaender et al., 2020) was included as positive control (Figures 1A and 1B). We first confirmed that cDNA transfection of these controls did not stimulate IFN signaling per se, as cells transfected with *CAT*, *GFP*, or *LY6E* expression plasmids show comparable levels of IFN-induced *ISG54* mRNA as mock-treated cells (Figure S1D). Screens were then conducted in duplicate and showed good reproducibility, with a Pearson correlation coefficient (r) of 0.81 (Figure 1C). After applying the cutoff criteria for infection (log2FC lower than 4 x standard deviations (SD) of CATlog2FC) and cell viability (at least 70% of CAT), we identified 65 ISGs that inhibited SARS-CoV-2 replication (Figure 1B). This list of antiviral factors includes upstream regulators as well as downstream effectors of the IFN response. The former include the signaling adaptor *MYD88*, signal transducers *STAT1* and *STAT2*, helicase *DDX60*, and E3 ubiquitin ligase *TRIM21*, all

---

(G) Differentiated HTBE cells stably expressing the indicating ISGs or negative control GFP were infected with SARS-CoV-2 (MOI = 1) on the apical side. At 18 h post-infection, supernatants were collected and the amount of SARS-CoV-2 focus-forming units per milliliter (FFU/mL) analyzed using Vero E6 cells. Data show mean ± SD and are representative from two sets of HTBE cells per ISG (n = 2).

Statistical significance was calculated using one-way ANOVA with Sidak's multiple comparison post hoc test (D) or one-way ANOVA with Dunnett's post hoc test (F and G).

of which were shown to stimulate *ISG54* production upon expression (Figure S1E). Conversely, we found several downstream effectors, including *BST2*, *IFITM2*, and *IFITM3*, which likely harbor direct antiviral activities and accordingly did not result in *ISG54* stimulation (Figure S1E). Cross-comparison of these 65 factors with published datasets of upregulated genes from COVID-19 patient samples and *in-vitro*-infected lung cell models revealed a small but significant overlap (Figure S1F), suggesting that a subset of these factors are also stimulated in response to SARS-CoV-2 infection (Blanco-Melo et al., 2020; Emanuel et al., 2020; Overmyer et al., 2020; Sun et al., 2020). The full list of identified ISGs and their activities are shown in Table S2.

To further validate the antiviral activity of the ISGs identified in this screen, we generated stable cell lines expressing each of these 65 ISGs fused with a C-terminal V5 affinity tag and assessed their ability to inhibit SARS-CoV-2 replication. Upon transduction of 293T-ACE2 cells with lentiviruses carrying these 65 factors, 7 cell lines did not survive antibiotic selection, so stable lines could only be generated for the remaining 58 ISGs. These lines were then evaluated for their ability to support SARS-CoV-2 replication, as well as for ISG expression. Of the 58 lines tested, 37 showed statistically significant reductions of SARS-CoV-2 replication compared to parental cells (log2FC $< 4 \times$ SDs of parental cells, and p value ≤ 0.05) (Figures 1D and 1E; Table S3), all of which showed detectable levels of each ISG as measured by V5 immunostaining (average percentage of $V5^{+}$ cells = 68.86%; Figure S1G). Among the ISGs that resulted in the highest reduction of SARS-CoV-2 replication was the transcription factor *ELF1* (normalized percentage of infection compared to control = 0.059, p value $<$ 0.0001; Table S3). Previous work showed that *ELF1* governs a complex transcriptional antiviral program of over 300 genes and restricts replication of several viruses (Seifert et al., 2019). To further evaluate if the identified antiviral ISGs exert direct antiviral activities or transcriptionally induce an antiviral response, we measured if their expression stimulate *ISG54* production. In addition to *ELF1*, overexpression of C-type lectin *CLEC4D*, the E3 ubiquitin ligase *TRIM21*, and the transcription factor *REC8* resulted in a significant increase in *ISG54* mRNA levels (Figure S1H), suggesting that these factors likely exert indirect antiviral activities.

Next, to assess if these ISGs inhibit viral replication in cell types more relevant for SARS-CoV-2 infection, we generated epithelial lung Calu-3 cells stably expressing a subset of these validated ISGs selected based on their reported function and their antiviral potencies (Table S3). From the 11 lines generated, 9 showed a significant reduction in SARS-CoV-2 replication compared to parental cells (Figure 1F). Subsequently, we used nine of these ISG-encoding lentiviruses to transduce primary HTBE cells. Each line was then differentiated at an air-liquid interface to produce a mucociliary epithelium similar to that of the native human airway (Rayner et al., 2019; Zaderer et al. 2019). Cells transduced with *CLEC4D*, *DNAJC6*, *B4GALT5*, *BST2*, and *UBD* showed reduced viability after antibiotic selection and so were excluded from further analysis. Cells expressing the remaining four ISGs (*CNP*, *APOL2*, *IFIT3*, and *RAB27A*) were infected with SARS-CoV-2 and evaluated for their ability to support viral growth. All these four lines showed a significant reduction in viral growth relative to control cultures transduced with GFP (Figure 1G). Together, these results suggest that a subset of these factors exert antiviral activities in several cellular backgrounds.

A network model of SARS-CoV-2 antiviral effectors

ISGs are a heterogenous group of genes with encoded functions ranging from inflammatory pathway signaling to intracellular trafficking, energy metabolism, and nuclear transport (Schoggins et al., 2011). To better understand the biochemical and functional context by which these 65 ISGs exert antiviral activities, we conducted a supervised network propagation leveraging high-confidence protein-protein interactions and hierarchical relationships (Figure 2; see STAR Methods). These network propagation studies are an important exercise to identify and highlight biological signals within a dataset. Thus, these analyses were included in this study to enable interpreting the proteins that showed antiviral activities in the context of other cellular components or molecular networks in which they might function during viral infection (Table S4). Using these analyses, we identified densely interconnected protein clusters that have significant enrichment in specific cellular biological processes (Raudvere et al., 2019). As expected, we found strong association with pathways that stimulate IFN signaling, including cytosolic PRRs (p value = 8.553×10^{-5}) and regulators of STAT phosphorylation (p value = 1.542×10^{-23}), as well as pathways linked to the type I IFN response (p value = 1.573×10^{-23}), the cellular response to viral infection (p value = 8.891×10^{-19}), and cytokine signaling (p value = 1.588×10^{-9}) (Figure 2A, blue boxes). We also observed an enrichment of RNA helicases (p value = 5.430×10^{-4}) and regulators of cell death (p value = 9.754×10^{-8}) (Figure 2A). These include *DDX60*, which exhibits antiviral activity against hepatitis C virus (HCV) and VSV (Schoggins et al., 2011); *ZBP1*, which was recently identified as a sensor of influenza A virus (IAV) Z-RNA motifs; and *MKLK*, a ZBP1 binding partner and downstream activator of necroptosis in response of viral infection (Figure 2B) (Zhang et al., 2020). Additional enriched clusters included regulation of transport at the Golgi network or the ER (p value = 7.423×10^{-5}, 3.574×10^{-4}) (Figures 2C and 2D), nucleotide metabolism (p value = 8.633×10^{-14}), and regulators of sphingolipid metabolism (p value = 2.093×10^{-6}), including the ISGs *B4GALT5* and *ST3GAL4* (Figure 2E). Additional ER/Golgi-resident factors identified as potent restrictors of SARS-CoV-2 replication included the apolipoprotein *APOL2*, previously shown to be important for lipid metabolism (Monajemi et al., 2002; Page et al., 2001); and *RSAD2/Viperin*, which is involved in lipid synthesis and control of ER membrane curvature and localizes to lipid droplets (Hinson and Cresswell, 2009; Seo and Cresswell, 2013), and has been suggested to inhibit HCV replication by altering the lipid composition at the ER compartment and disrupt lipid rafts to inhibit IAV growth (Fitzgerald, 2011). This suggests that regulation of the membrane composition at sites relevant for viral replication or trafficking could be a critical host strategy for the control of SARS-CoV-2 replication. However, additional work will be required to characterize how these ISGs inhibit SARS-CoV-2 replication. Taken together,

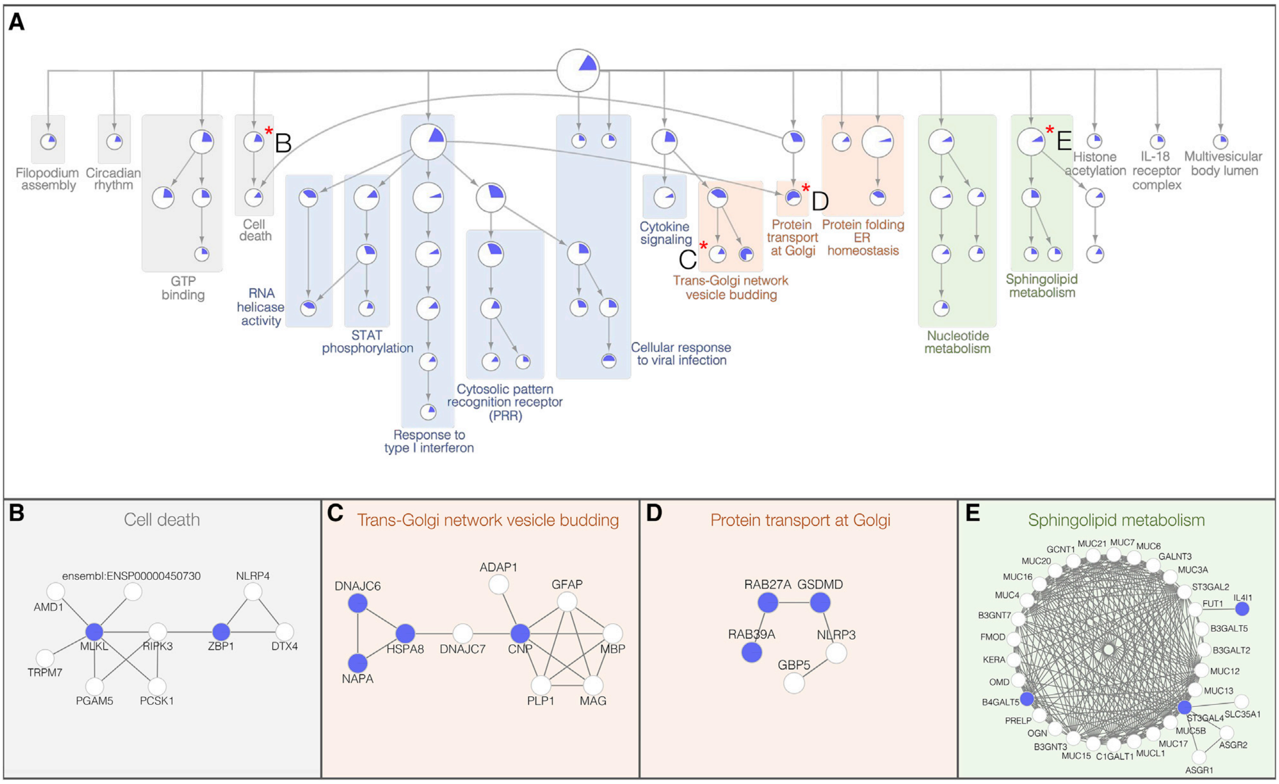

Figure 2. Network model of SARS-CoV-2 antiviral effectors

(A) The network containing the 65 identified antiviral ISGs was propagated to include a total of 343 high-confidence protein interactors (score > 0.7 STRING) and subjected to supervised community detection (Carlin et al., 2017; Shannon et al., 2003). The resultant hierarchy is shown. Here, each node represents a community of densely interconnected proteins, and each edge (arrow) denotes containment of one community (edge target) by another (edge source). Enriched biological processes are indicated. The percentage of each community that corresponds to the 65 antiviral ISGs is shown in dark blue.

(B–E) Zoom-in insets from selected protein communities are indicated with an asterisk (*) in the hierarchy. Nodes indicate proteins, and edges indicate interactions from STRING. Blue nodes indicate ISGs that restricted SARS-CoV-2 replication.

this network model illuminates the diversity of cellular activities that likely function to mount an antiviral response to SARS-CoV-2 replication. Further investigation of these molecular pathways that underlie innate immune control of viral infection can provide further insight into cellular strategies designed to inhibit viral replication and growth.

Restriction of SARS-CoV-2 entry

To understand how these antiviral effectors impact viral replication, the 37 validated ISGs (Figure 1D) were tested for their ability to inhibit specific stages of the SARS-CoV-2 infectious cycle. First, we used a pseudotyped VSV expressing SARS-CoV-2 S protein (VSV-S), alongside a second VSV expressing its natural glycoprotein (VSV-G), to measure viral entry (Figure 3A). Second, we assessed viral translation and RNA replication by measuring viral RNA at 8 h post-infection (Figure 3B). Lastly, we infected naive cells with viral supernatants that were collected at 18 h post-infection to assess late-stage activity, which encompasses viral assembly and egress (Figure 3C). These experimental data were integrated with manually curated bioinformatic resources that provide information on subcellular localization and membership to biological pathways in order to establish a visual model that predicts the impact of these ISGs on the SARS-CoV-2 infectious cycle (Figure 4).

Entry of SARS-CoV-2 into the host cell is facilitated by viral S protein binding to the ACE2 cellular receptor promoting endocytosis. Upon entry, SARS-CoV-2 viral particles escape the endosome to initiate viral replication (Hoffmann et al., 2020). Six ISGs reduced entry of the pseudotyped VSV-S by more than 50% compared to parental cells, including *LY6E*, *CLEC4D*, *UBD*, *ELF1*, *FAM46C*, and *REC8* (Figures 3A and 4). Of these, *CLEC4D*, *ELF1*, and *REC8* promoted induction of *ISG54* expression (Figure S1H). Both *ELF1* and *CLEC4D* have been shown to inhibit pathogen replication by controlling production of ISGs and cytokines ((Seifert et al., 2019; Wilson et al., 2015). Thus, these data suggest that these factors act as indirect negative regulators of viral infection through a secondary antiviral transcriptional cascade that acts to inhibit SARS-CoV-2 entry and potentially other stages of the viral life cycle. Interestingly, all three factors also affected entry of VSV-G (Figure S2A), suggesting that the antiviral programs they control likely affect replication of other RNA viruses.

ISGs that also reduced entry of VSV-S were *LY6E*, *UBD*, and *FAM46C* (Figure 3A). Overexpression of these factors did not significantly induce *ISG54* production (Figure S1H), suggesting

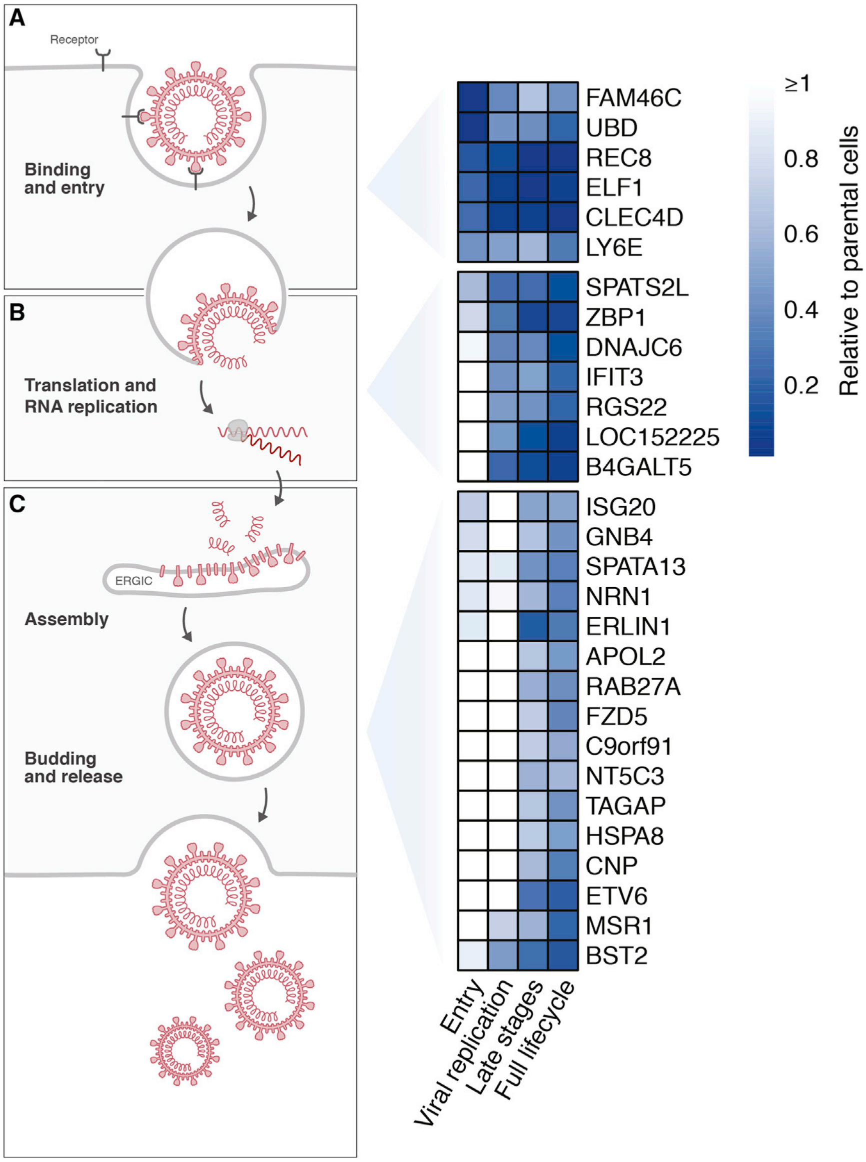

Figure 3. SARS-CoV-2 antiviral effectors inhibit discrete viral replication steps

(A–C) 293T-ACE2 cells stably expressing each of the indicated ISGs were subjected to (A) infection with SARS-CoV-2 pseudotyped VSV luciferase virus for 16 h prior to measurement of luciferase signal. In parallel, cells were subjected to synchronized infection with SARS-CoV-2 (MOI = 4) for 6 h prior to measurement of viral RNA (B), or supernatants at 18 h post-infection were used to infect naive Vero E6 cells. The percentage of infected cells was then determined at 18 h post-infection using immunostaining for viral N protein (C). In parallel to these experiments, the impact of these ISGs on SARS-CoV-2 replication at 24 h post-infection was evaluated (full life cycle). Results are summarized in the heatmap and show the mean (n = 2) of relative activities compared to parental cells.

they might directly inhibit viral entry. *FAM46C* showed no effect on VSV-G (Figure S2A), indicating it could target a specific feature of S-mediated entry. Notably, *LY6E* and *UBD* showed a contrasting ability to reduce entry of VSV-S but increase that of VSV-G (Figure S2A). *LY6E* was previously shown to restrict entry of live SARS-CoV-2 by inhibiting viral S protein fusion at the membrane (Pfaender et al., 2020) and to act as a proviral entry factor for other RNA viruses, including IAV or flaviviruses (Hackett and Cherry, 2018; Mar et al., 2018). Similarly, *UBD/FAT10* is recruited to the incoming Salmonella-containing vacuole (SCV) together with the autophagy cargo receptor p62 (Spinnenhirn et al., 2014), which serve as signals for lysosomal targeting and pathogen clearance, but acts as a proviral factor for IAV replication (Nguyen et al., 2016). More work will be required to investigate how UBD interferes with SARS-CoV-2 entry.

Cellular inhibition of SARS-CoV-2 translation and RNA replication

Following SARS-CoV-2 release into the cytosol, the transcription and translation of the replicase gene from the viral genomic RNA generates nonstructural proteins (nsps). These nsps coordinate the assembly of the replicase-transcriptase complex (RTC) at the ER, which enables viral RNA replication and protein synthesis (Fehr and Perlman, 2015). Seven ISGs were found to reduce SARS-CoV-2 RNA levels by more than 50% (Figure 3B), including *IFIT3*, *SPATS2L*, *DNAJC6*, *RGSS2*, and LOC152225, as well as *ZBP1* and *B4GALT5*, which were found to be core components of the cell death and sphingolipid metabolism networks shown in Figures 2B and 2E.

The IFIT family includes five members (*IFIT1*, *IFIT1B*, *IFIT2*, *IFIT3*, and *IFIT5*), which prevent active viral RNA replication by detection and sequestering of single-stranded 5′-ppp or 2′O-unmethylated RNA (Metz et al., 2013). In this study, we identified three members of this family, *IFIT1*, *IFIT3*, and *IFIT5*, to inhibit SARS-CoV-2 replication (Figure 3B), suggesting this family plays an important role in the restriction of SARS-CoV-2. Viral RNA levels were also reduced by the RNA binding protein SPAT2SL (Figure 3B). Following stress stimuli, SPAT2SL is recruited to cytoplasmic stress granules, where viral RNA can be sequestered to reduce viral genome synthesis (Miller, 2011; Zhu et al., 2008). Finally, the ISG *DNAJC6*, a member of the heat shock protein 40 (HSP40) family, was also determined to impact the SARS-CoV-2 replicative stage (Figure 3B). *HSP40* family members are known to play critical roles in protein transport, folding, and structural disassembly and have been found to bind the 3′ untranslated region of the mouse hepatitis virus (MHV) coronavirus

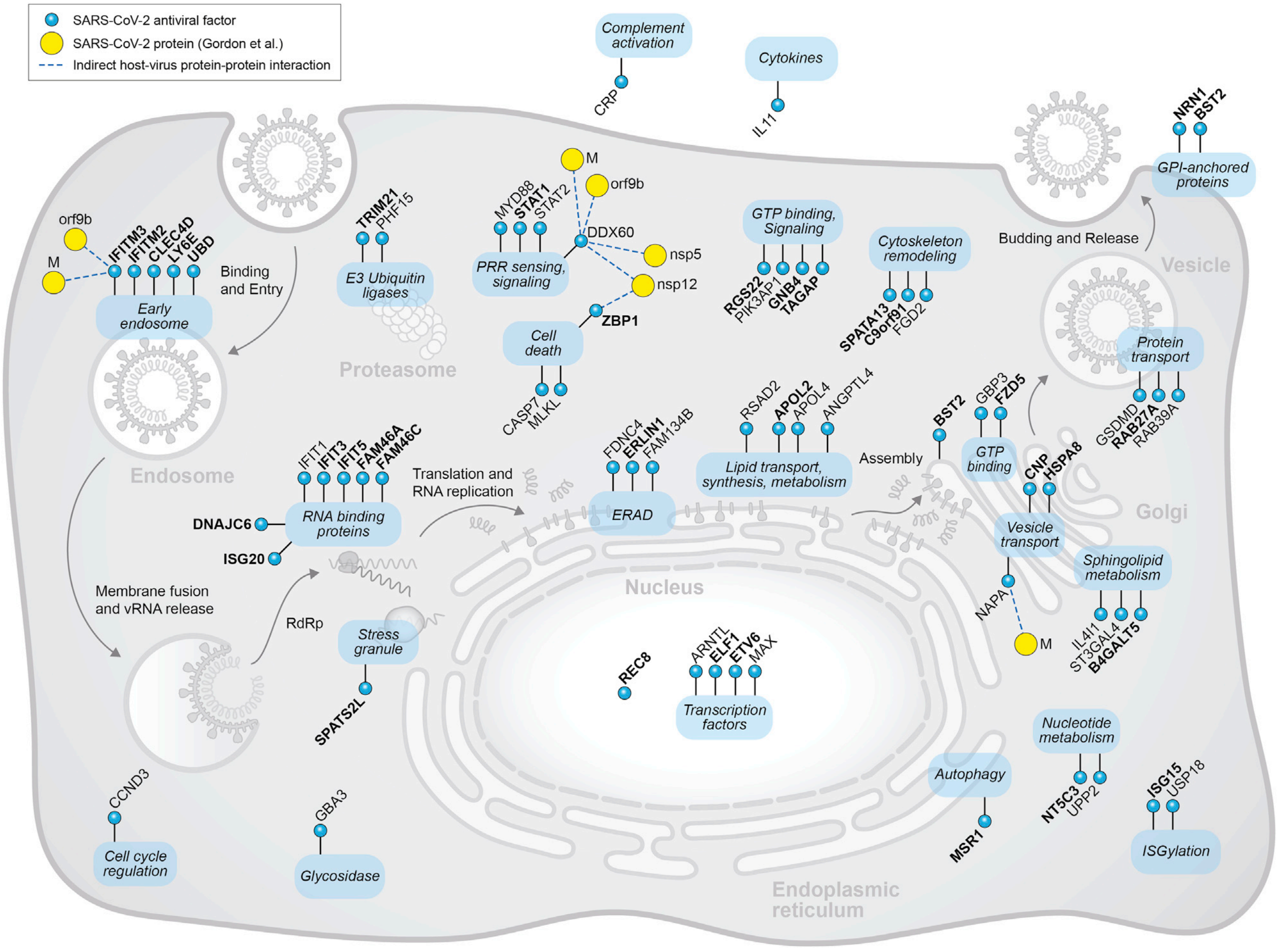

Figure 4. Integrated model of SARS-CoV-2 cellular restriction mechanisms

ISGs that inhibited SARS-CoV-2 replication were placed at specific positions along the viral infectious cycle based on experimental data generated in Figure 3 in conjunction with Gene Ontology, KEGG, and Reactome databases and the literature (see STAR Methods). Human ISGs are represented in blue circles and SARS-CoV-2 proteins in yellow circles. ISGs in bold indicate those ISGs that were validated using lentiviral transduction (Figure 1D). Dashed lines (edges) represent indirect interactions between these ISGs and the indicated viral proteins based on reported ISG interactors (Hubel et al., 2019) and SARS-CoV-2 interactors (Gordon et al., 2020).

(Nanda et al., 2004; Rosenzweig et al., 2019). Overall, these data suggest that molecular recognition and targeting of viral RNA could be a critical host defense strategy used to interfere with SARS-CoV-2 translation or genome synthesis (Figure 4).

ER- and Golgi-resident ISGs inhibit late-stage SARS-CoV-2 replication

Transcription and translation of SARS-CoV-2 subgenomic mRNAs at the ER membrane generate accessory, as well as the structural proteins S, envelope (E), membrane (M), and N. S, E, and M are then inserted into the ER and transit through the secretory pathway to commence viral assembly in the ER-Golgi intermediate compartment (ERGIC). Specifically, M, S, and E associate with viral genomes encapsidated by the N protein to form virions that bud from the ERGIC. Virions traffic in vesicles through the *trans*-Golgi network and are subsequently released by exocytosis. Notably, we found that the majority of ISGs in this assay (16/35, 55%) restricted late stages of viral replication (Figure 3C). These late-stage ISGs were then clustered based on their known impact on ERAD and vesicle trafficking pathways.

ERAD. Accumulation of viral proteins during virion assembly at the ER-Golgi interface can trigger ERAD. Accordingly, we found that the ERAD regulator *ERLIN1* (Pearce et al., 2009) strongly attenuated late stages of SARS-CoV-2 replication (Figure 3C). Two additional factors, *RETREG1* and *FNDC4*, also involved in this pathway with roles as a ER-phagy receptor and association with the aggresome (Mo et al., 2020; Wilkinson, 2019), were also found to restrict SARS-CoV-2 replication (Figures 3C and 4), suggesting that factors associated with the ERAD pathway could act as inhibitors of SARS-CoV-2 infection.

Vesicle trafficking.Trans-Golgi vesicle budding was found to be an enriched pathway involved in SARS-CoV-2 restriction (Figure 2C). Proteins within this network include the heat shock protein *HSPA8* and the 2′,3′-cyclic nucleotide 3′ phosphodiesterase *CNP*; both mapped to late-stage viral replication (Figure 3C).

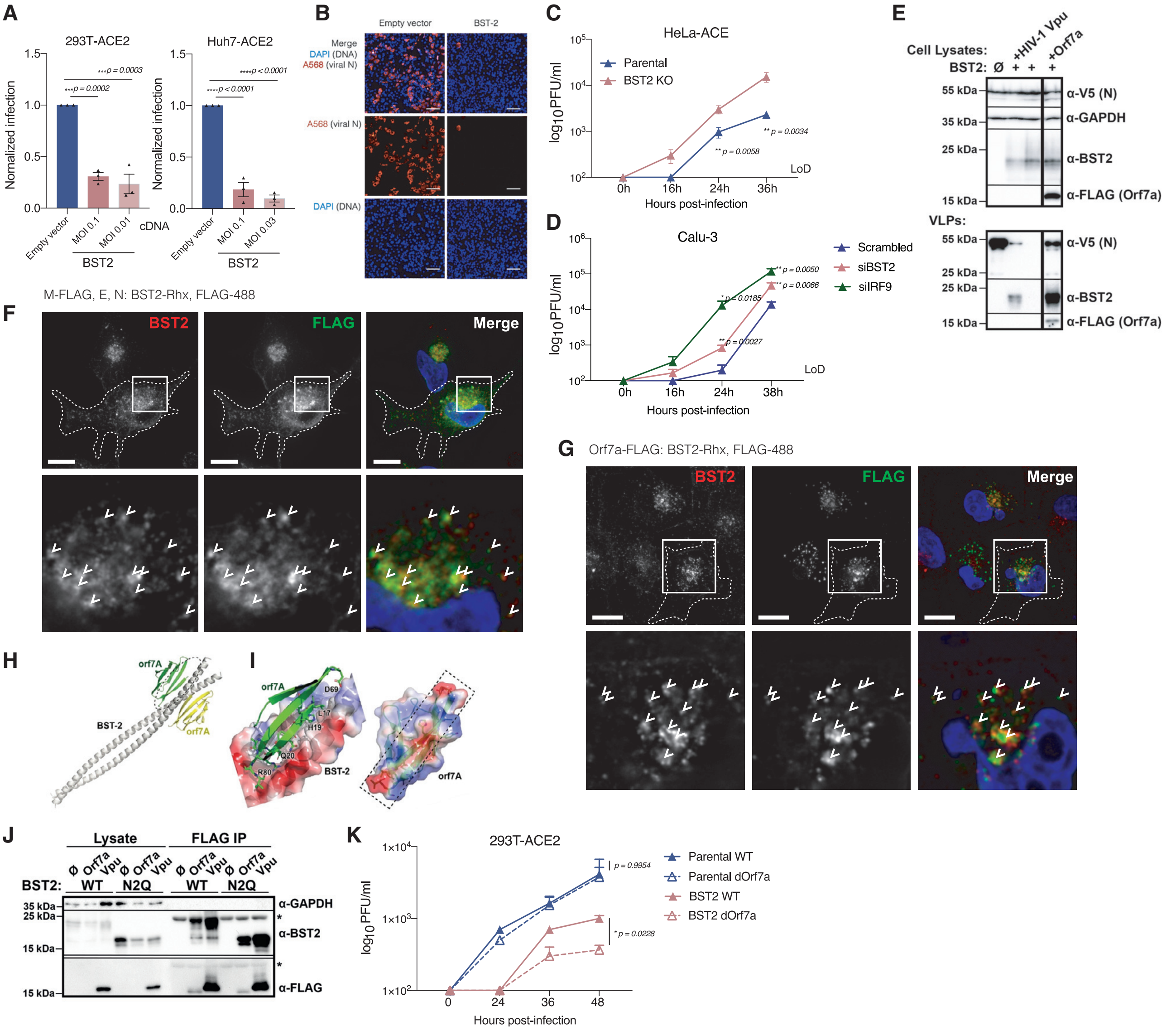

Figure 5. BST2 inhibits release of SARS-CoV-2 and is antagonized by Orf7a

(A and B) 293T and Huh7 cells transfected with BST2 along with ACE2 and TMPRSS2 were infected with SARS-CoV-2 at the indicated MOIs for 48 h prior to immunostaining for viral N protein. Shown is mean ± SEM normalized infection (percentage of SARS-CoV-2 N^+ cells) relative to empty vector control from three independent experiments (n = 3) (A) and representative images of Huh7 cells infected at MOI 0.03 (B).

(C) HeLa-ACE2 parental or BST2 KO cells were infected with SARS-CoV-2 (MOI = 2). At the indicated hours post-infection, supernatants were collected and analyzed by plaque assay in Vero E6 cells. LoD, limit of detection. Data show mean ± SD from one representative experiment in triplicate (n = 3) of two independent experiments.

(D) Calu-3 cells were transfected with siRNAs targeting BST2 or IRF9 or the negative control scrambled siRNA. At 48 h post-transfection, cells were treated with 18 IU/mL IFN for 6 h and then infected with SARS-CoV-2 (MOI = 0.75). At indicated times post-infection, supernatants were collected and analyzed by plaque assay in Vero E6 cells. Data show mean ± SD and are representative from one experiment in quadruplicate (n = 4).

(E) 293T cells were transfected with the indicated constructs for 24 h. Cell lysates and supernatants (VLPs) were then analyzed using SDS-PAGE and immunoblotted with indicated antibodies. Only blot lanes 2–4 and 6 (shown in boxes) are relevant to this experiment and included in the figure.

(F) HeLa-ACE2 cells transfected with M-FLAG, E, and N were subjected to immunostaining for BST2 and FLAG, as indicated. Shown are deconvolved widefield microscopic images revealing colocalization of BST2 and M (arrows). Scale bars, 10 μm.

(G) HeLa-ACE2 cells transfected with Orf7a-FLAG were subjected to immunostaining for BST2 and FLAG, as indicated. Shown are confocal images revealing colocalization of BST2 and Orf7a (arrows). Scale bars, 10 μm.

(H) Top two ClusPro docking models of Orf7a interaction with the BST-2 ectodomain dimer. BST-2 is shown in gray, and the two Orf7a molecules are green and yellow.

(legend continued on next page)

HSPA8 is known to be involved in vesicle uncoating, whereas *CNP* was reported to inhibit release of human immunodeficiency virus 1 (HIV-1) (Wilson et al., 2012). Notably, these ISGs were found in a protein complex with *NAPA* (Figure 2C), also identified as restriction factor for soluble NSF-attachment protein receptor (SNARE) complex, and a reported member of the soluble NSF-attachment protein receptor (SNARE) complex that functions to dock and fuse vesicles to target membranes (Inoue et al., 2015). Finally, the GTPase *Rab27a* also impeded late stages of replication. *Rab27a* controls exocytic transport through fusion of multivesicular endosomes to the plasma membrane (Ostrowski et al., 2010), further underscoring the role of factors involved in vesicular trafficking as critical negative regulators of SARS-CoV-2 replication.

BST2 inhibits release of SARS-CoV-2 and is antagonized by Orf7a

The bone marrow stromal antigen 2 (BST2; also known as CD317 or tetherin) was identified as a potent inhibitor of SARS-CoV-2 replication (Figure 3C). BST2 traffics through the ER and Golgi and localizes at the plasma membrane and in endosomes. It has been shown to inhibit viral release of several enveloped viruses, including HIV-1, human coronavirus 229E, and SARS-CoV-1, that either bud at the plasma membrane or at the ERGIC, by tethering their virions to the cell surface or intracellular membranes (Neil et al., 2008; Taylor et al., 2015; Van Damme et al., 2008; Wang et al., 2014).

BST2 restriction of SARS-CoV-2 replication was further confirmed in ACE2/TMPRSS2-expressing 293T and Huh7 cells at 24 and 48 h post-infection (Figures 5A, 5B, and S3A). We next conducted loss-of-function studies in HeLa cells, as these cells constitutively express BST2 (Neil et al., 2008; Van Damme et al., 2008), and found that cells depleted for BST2 released significantly more infectious viruses over time (Figures 5C and S3B). We further validated this observation using human lung epithelial cells, since knockdown of BST2 in Calu-3 cells resulted in a significant increase in SARS-CoV-2 titers at 24 and 38 h post-infection (Figures 5D, S3C, and S3D). Overall, these data strongly support a role for BST2 in the restriction of SARS-CoV-2 replication.

Notably, BST2 expression reduced SARS-CoV-2 RNA replication (53% reduction compared to control cells) followed by a more potent reduction of viral release (74% reduction) (Figures 3B and 3C). To further characterize the impact of BST2 on late-stage replication, we evaluated viral egress in the presence or absence of BST2 using a virus-like particle (VLP) system that bypasses viral entry and viral RNA replication (Siu et al., 2008). We confirmed that this system can recapitulate virus egress, as transfection of viral M, N, and E, but not E and N or M and N, resulted in secreted N protein (Figure S3E). Using this system, we detected a strong reduction of VLP release in the presence of BST2, evidenced by loss of secreted N, corroborating that BST2 acts to inhibit egress of SARS-CoV-2 (Figure 5E). We next investigated if BST2 colocalizes with SARS-CoV-2 structural proteins. Notably, we detected colocalization of BST2 and structural proteins M (Figure 5F) and S (Figure S3F) at intracellular foci. Together, these data indicate that BST2 spatially associates with SARS-CoV-2 structural proteins.

Several viruses have developed evasion strategies to overcome restriction by BST2, including HIV-1 via its accessory protein Vpu and SARS-CoV-1 via its Orf7a and S proteins (Neil et al., 2008; Taylor et al., 2015; Van Damme et al., 2008; Wang et al., 2019). Notably, we found that both HIV-1 Vpu and SARS-CoV-2 Orf7a expression partially rescued BST2-mediated inhibition of SARS-CoV-2 release (Figure 5E) and that both Orf7a and BST2 were incorporated into VLP particles (Figure 5E) (Fitzpatrick et al., 2010). Notably, Orf7a-mediated antagonism of BST2 activity did not involve reduction of BST2 cell surface expression, in contrast to HIV-1 Vpu (Figure S3G). We further investigated the location of BST2 and Orf7a in the cell and observed that BST2 and Orf7a colocalized in the perinuclear region (Figure 5G). *In silico* docking of SARS-CoV-2 Orf7a and BST2 revealed a potential interface at the N-terminal region of BST2 ectodomain (Figures 5H and 5I), suggesting that these two proteins could physically interact. To evaluate this hypothesis, we assessed BST2 and Orf7a interaction through immunoprecipitation studies. These were conducted using wild type (WT) or a BST2 mutant defective for N-linked glycosylation (N2Q), as a previous report suggested that the interaction between SARS-CoV-1 Orf7a and BST2 was glycosylation dependent (Taylor et al., 2015). In contrast to SARS-CoV-1, these data revealed an association between SARS-CoV-2 Orf7a and BST2 independently of BST2 glycosylation status (Figure 5J).

To further investigate Orf7a antagonism of BST2, we infected parental or 293T-ACE2 cells stably expressing BST2 with either WT SARS-CoV-2 or a recombinant SARS-CoV-2 that was engineered to replace Orf7a with nanoluciferase (dOrf7a) (kindly provided by Ralph Baric) (Hou et al., 2020). While WT and dOrf7a viruses grew similarly in parental cells (Figure 5K) and showed comparable levels of SARS-CoV-2 N protein (Figure S3H), the replication of dOrf7a virus was significantly attenuated in BST2-expressing cells at 48 h post-infection (Figure 5K). Overall, these data establish BST2 as a potent inhibitor of SARS-CoV-2 egress and demonstrate that viral Orf7a protein enables immune evasion through the antagonism of BST2 restriction.

(I) Close-up of the interface circled in H. Left: electrostatic surface of BST2 (blue, positive; red, negative). Beta strands A and G of Orf7a (green) are involved in the interaction. Selected interaction residues are labeled. Right: electrostatic surface of Orf7a. The beta strands A and G form an electrostatic ridge on the surface (boxed).

(J) 293T cells were transfected with BST2 expression plasmid (WT or N2Q mutant) and empty plasmid, Orf7a-FLAG, or HIV-1 Vpu-FLAG expression plasmid. Immunoprecipitation (IP) was carried out using FLAG M2 magnetic beads. Inputs and IP samples were analyzed by SDS-PAGE using indicated antibodies. Blot is representative from two independent experiments. The asterisks (*) denote the 25-kDa anti-FLAG (M2) light chain.

(K) Parental 293T-ACE2 or BST2 stable cells were infected with WT or dOrf7a (MOI = 1). At indicated times post-infection, supernatants were collected and analyzed by plaque assay in VeroE6 cells. Data show mean ± SD from one representative experiment in triplicate (n = 3) of two independent experiments. Statistical significance was calculated using one-way ANOVA with Dunnett's post hoc (A and D), Student's t test (C), or Tukey's multicomparison test (K).

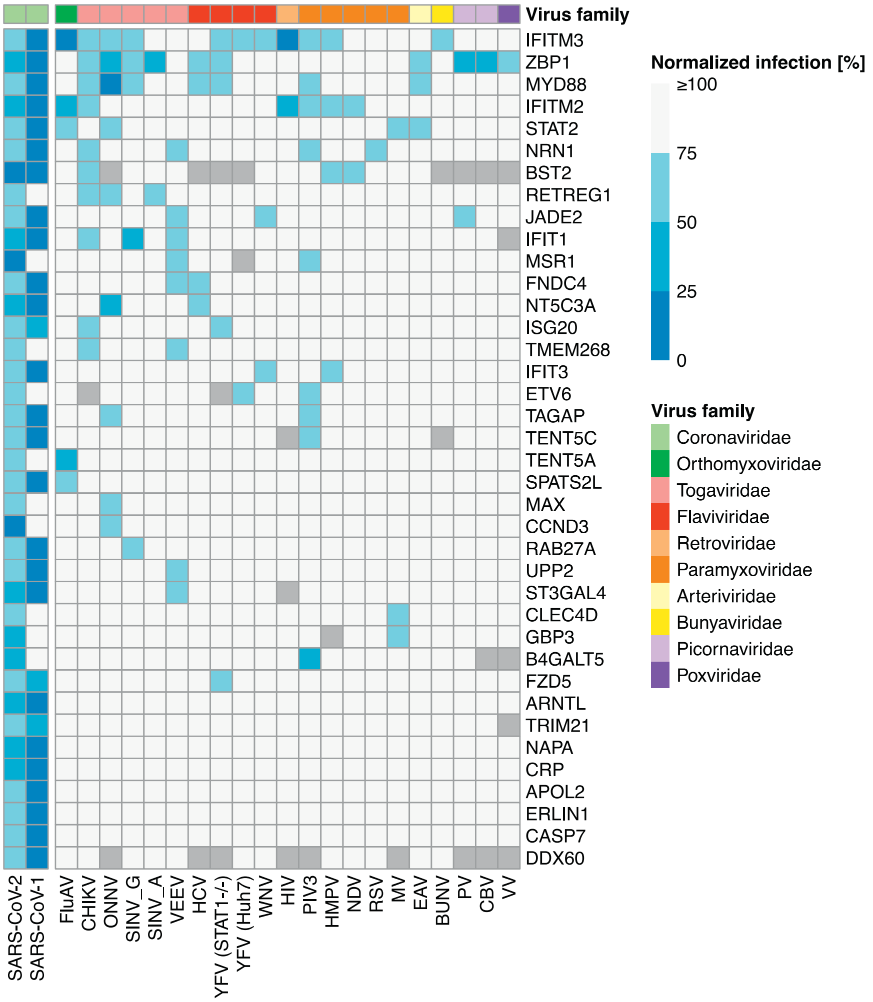

Figure 6. Comparative antiviral activities of SARS-CoV-2 restriction factors

Heatmap showing normalized infection upon overexpression of indicated ISGs across 21 viruses. Data for SARS-CoV-2 were generated within this study (see Table S2). Data for the remaining 20 viruses were obtained from previously published work (Schoggins et al., 2011, 2014). Data for SARS-CoV-1 were generated by infecting 293T-ACE2 stably expressing each of the indicated ISGs with SARS-CoV-1 (MOI = 0.01). At 48 h post-infection, supernatants were collected and used to calculate the median tissue culture infectious dose (TCID50). Data show TCID50/mL relative to parental control wells. Data show mean ± SD from one representative experiment in triplicate (n = 3) of two independent experiments. Virus families are indicated. Virus full names and abbreviations are described in STAR Methods.

Comparative antiviral activities of SARS-CoV-2 restriction factors

Finally, to understand if discrete cellular defense strategies are deployed to inhibit SARS-CoV-2 replication, the restriction dataset was cross-referenced with published single ISG overexpression studies that covered 20 different RNA and DNA viruses, including IAV (FluAV), West Nile virus (WNV), HCV, and HIV-1 (Schoggins et al., 2011, 2014) (Figure 6). In addition, we experimentally evaluated if expression of these factors could inhibit the replication of SARS-CoV-1 (Figure 6). Ten anti SARS-CoV-2 ISGs were found to reduce replication of four or more viruses (Figure 6). These include well-described IFN signaling transducers, signaling molecules, and innate immune sensors, including *STAT2* and *MYD88*, the inhibitors of viral entry *IFITM2* and *IFITM3* (Brass et al., 2009), and the viral nucleic acid binders *ZBP1* and *IFIT1*. Conversely, a cluster of eight ISGs harbored selective activities for SARS-CoV-2 (Figure 6), all of which also inhibited SARS-CoV-1 replication and include the ER/Golgi-resident proteins *NAPA*, *APOL2*, and *ERLIN1*. Notably, significant enrichment in ISGs that regulate ER homeostasis and Golgi transport suggest that these organelles are critical sites for the cellular control of SARS-CoV replication. Surprisingly, many of these antiviral factors have not been reported to impact other viruses that rely on these membraned compartments for replication and assembly, including flavi-, toga-, arteri-, and bunyaviruses, suggesting that these cellular defense mechanisms target unique aspects of coronavirus replication, assembly, and egress.

Taken together, this comprehensive analysis of the ISGs that act to impede SARS-CoV-2 revealed that the IFN response to SARS-CoV-2 infection relies on a limited subset of ISGs that govern a diverse set of cellular functions, including endocytosis, nucleotide biosynthesis, and sphingolipid metabolism. Further dissection of these critical host-pathogen interactions, as well as potential viral evasion strategies, will enable insights into the molecular determinants of innate immune control of SARS-CoV-2 replication and their role in clinical disease outcome.

Limitations of study

This study investigated the cellular innate immune control of SARS-CoV-2 replication by evaluating the ability of ISGs to inhibit viral replication. These ISGs were selected based on RNA-seq analysis of human lung cells treated with IFN. However, we cannot exclude that IFN treatment *in vivo* can induce an additional subset of ISGs that were not evaluated in this study. From the 399 ISGs tested, 65 were found to control viral infection in human cells. Since the expression levels of the remaining 334 ISGs were not recorded, it is possible that the cellular restriction of SARS-CoV-2 relies on additional ISGs that were not illuminated in this study. Future studies should evaluate whether these ISGs act to inhibit viral replication *in vivo* and their role during clinical infection.

STAR★METHODS

Detailed methods are provided in the online version of this paper and include the following:

SUPPLEMENTAL INFORMATION

Supplemental information can be found online at https://doi.org/10.1016/j.molcel.2021.04.008.

ACKNOWLEDGMENTS

We would like to thank Ralph Baric for providing the dOrf7a SARS-CoV-2, Thomas Rogers for the HeLa-ACE2 cells, Kwok-Yung Yuen for the rabbit-anti-SARS-CoV-2 N antibody, and Stefan Pohlmann for the mammalian expression vector encoding SARS-CoV-2 S and pCG1-CoV2-S-HA. We thank Marisol Chacon for administrative support and Sylvie Blondelle and Larry Adelman for biosafety support. We would also like to thank the Viral Vector Core Facility at SBP for cDNA normalization and lentivirus production. This work was supported by the following grants to the SBP Medical Discovery Institute and the Icahn School of Medicine at Mount Sinai: DOD W81XWH-20-1-0270, DHIPC U19 AI118610, and Fluomics/NOSI U19 AI135972. This work was also supported by generous philanthropic donations from Dinah Ruch and Susan & James Blair, the JPB Foundation, the Open Philanthropy Project (research grant 2020-215611 (5384)), and anonymous donors. Additional support has been provided by DARPA (grant HR0011-19-2-0020) and CRIP (Center for Research on Influenza Pathogenesis), a NIAID-funded Center of Excellence for Influenza Research and Surveillance (CEIRS; contract HHSN272201400008C). This work was additionally supported by the following grants to Northwestern University Feinberg School of Medicine: a CTSA supplement to NCATS (UL1 TR002389), a CTSA supplement to NUCATS with the generous support of the Dixon family (UL1 TR001422), and a Cancer Center supplement (P30 CA060553). Additional support was provided by NIH grant R37AI081668 to J.G. at UC San Diego and a generous grant from the James B. Pendleton Charitable Trust. The funding sources had no role in the study design, data collection, analysis, interpretation, or writing of the report. The content of this study is solely the responsibility of the authors and does not necessarily represent the official views of the NIH.

AUTHOR CONTRIBUTIONS

L.M.-S., M.K.L., C.A.S., J.G., and S.K.C. conceived and designed the experiments. L.M.-S., M.K.L., X.Y., C.A.S., A.P.G., P.D.J., C.N., Y.P., M.E.B., S.W., H.M.C., and A.L.O. conducted and/or analyzed the experiments. L.M.-S., L.P., and A.M.O. conducted data analysis and representation. A.R.-F., M.U., M.W.C., and C.B. performed and/or analyzed the RNA-seq experiments. L.M.-S., D.P., C.C., S.L., S.B.R., F.Z., and T.I. generated the network model. C.W. and Y.X. generated the *in silico* docking model. L.M. and J.F.H. generated essential reagents. L.M.-S. and S.K.C. wrote the manuscript with contributions from all authors. L.P., C.B., A.G.-S., and S.K.C. acquired funding.

DECLARATION OF INTERESTS

The authors declare no competing interests.

Received: September 17, 2020
Revised: February 1, 2021
Accepted: April 7, 2021
Published: April 13, 2021

REFERENCES

Arunachalam, P.S., Wimmers, F., Mok, C.K.P., Perera, R.A.P.M., Scott, M., Hagan, T., Sigal, N., Feng, Y., Bristow, L., Tak-Yin Tsang, O., et al. (2020). Systems biological assessment of immunity to mild versus severe COVID-19 infection in humans. Science *369*, 1210–1220.

Blanco-Melo, D., Nilsson-Payant, B.E., Liu, W.-C., Uhl, S., Hoagland, D., Møller, R., Jordan, T.X., Oishi, K., Panis, M., Sachs, D., et al. (2020). Imbalanced Host Response to SARS-CoV-2 Drives Development of COVID-19. Cell *181*, 1036–1045.e9.

Brass, A.L., Huang, I.-C., Benita, Y., John, S.P., Krishnan, M.N., Feeley, E.M., Ryan, B.J., Weyer, J.L., van der Weyden, L., Fikrig, E., et al. (2009). The IFITM proteins mediate cellular resistance to influenza A H1N1 virus, West Nile virus, and dengue virus. Cell *139*, 1243–1254.

Brooks, B.R., Brooks, C.L., 3rd, Mackerell, A.D., Jr., Nilsson, L., Petrella, R.J., Roux, B., Won, Y., Archontis, G., Bartels, C., Boresch, S., et al. (2009). CHARMM: the biomolecular simulation program. J. Comput. Chem. *30*, 1545–1614.

Carlin, D.E., Demchak, B., Pratt, D., Sage, E., and Ideker, T. (2017). Network propagation in the cytoscape cyberinfrastructure. PLoS Comput. Biol. *13*, e1005598.

Deprez, M., Zaragosi, L.-E., Truchi, M., Becavin, C., Ruiz García, S., Arguel, M.-J., Plaisant, M., Magnone, V., Lebrigand, K., Abelanet, S., et al. (2020). A Single-Cell Atlas of the Human Healthy Airways. Am. J. Respir. Crit. Care Med. *202*, 1636–1645.

Dutkowski, J., Kramer, M., Surma, M.A., Balakrishnan, R., Cherry, J.M., Krogan, N.J., and Ideker, T. (2013). A gene ontology inferred from molecular networks. Nat. Biotechnol. *31*, 38–45.

Emanuel, W., Kirstin, M., Vedran, F., Asija, D., Theresa, G.L., Roberto, A., Filippos, K., David, K., Salah, A., Christopher, B., et al. (2020). Bulk and single-cell gene expression profiling of SARS-CoV-2 infected human cell lines identifies molecular targets for therapeutic intervention. BioRxiv, 2020.05.05.079194.

Fehr, A.R., and Perlman, S. (2015). Coronaviruses: an overview of their replication and pathogenesis. Methods Mol. Biol. *1282*, 1–23.

Fitzgerald, K.A. (2011). The interferon inducible gene: Viperin. J. Interferon Cytokine Res. *31*, 131–135.

Fitzpatrick, K., Skasko, M., Deerinck, T.J., Crum, J., Ellisman, M.H., and Guatelli, J. (2010). Direct restriction of virus release and incorporation of the interferon-induced protein BST-2 into HIV-1 particles. PLoS Pathog. *6*, e1000701.

García-Sastre, A. (2017). Ten Strategies of Interferon Evasion by Viruses. Cell Host Microbe *22*, 176–184.

Gordon, D.E., Jang, G.M., Bouhaddou, M., Xu, J., Obernier, K., O'Meara, M.J., Guo, J.Z., Swaney, D.L., Tummino, T.A., Hüttenhain, R., et al. (2020). A SARS-CoV-2-Human Protein-Protein Interaction Map Reveals Drug Targets and Potential Drug-Repurposing. bioRxiv. https://doi.org/10.1101/2020.03.22.002386.

Hackett, B.A., and Cherry, S. (2018). Flavivirus internalization is regulated by a size-dependent endocytic pathway. Proc. Natl. Acad. Sci. USA *115*, 4246–4251.

Hadjadj, J., Yatim, N., Barnabei, L., Corneau, A., Boussier, J., Smith, N., Péré, H., Charbit, B., Bondet, V., Chenevier-Gobeaux, C., et al. (2020). Impaired type I interferon activity and inflammatory responses in severe COVID-19 patients. Science *369*, 718–724.

Hinson, E.R., and Cresswell, P. (2009). The antiviral protein, viperin, localizes to lipid droplets via its N-terminal amphipathic alpha-helix. Proc. Natl. Acad. Sci. USA *106*, 20452–20457.

Hoffmann, M., Kleine-Weber, H., Schroeder, S., Krüger, N., Herrler, T., Erichsen, S., Schiergens, T.S., Herrler, G., Wu, N.-H., Nitsche, A., et al. (2020). SARS-CoV-2 Cell Entry Depends on ACE2 and TMPRSS2 and Is Blocked by a Clinically Proven Protease Inhibitor. Cell *181*, 271–280.e8.

Hou, Y.J., Okuda, K., Edwards, C.E., Martinez, D.R., Asakura, T., Dinnon, K.H., 3rd, Kato, T., Lee, R.E., Yount, B.L., Mascenik, T.M., et al. (2020). SARS-CoV-2 Reverse Genetics Reveals a Variable Infection Gradient in the Respiratory Tract. Cell *182*, 429–446.e14.

Huang, C., Wang, Y., Li, X., Ren, L., Zhao, J., Hu, Y., Zhang, L., Fan, G., Xu, J., Gu, X., et al. (2020). Clinical features of patients infected with 2019 novel coronavirus in Wuhan, China. Lancet *395*, 497–506.

Hubel, P., Urban, C., Bergant, V., Schneider, W.M., Knauer, B., Stukalov, A., Scaturro, P., Mann, A., Brunotte, L., Hoffmann, H.H., et al. (2019). A protein-interaction network of interferon-stimulated genes extends the innate immune system landscape. Nat. Immunol. *20*, 493–502.

Hultquist, J.F., Hiatt, J., Schumann, K., McGregor, M.J., Roth, T.L., Haas, P., Doudna, J.A., Marson, A., and Krogan, N.J. (2019). CRISPR-Cas9 genome engineering of primary CD4$^+$ T cells for the interrogation of HIV-host factor interactions. Nat. Protoc. *14*, 1–27.

Hung, I.F.-N., Lung, K.-C., Tso, E.Y.-K., Liu, R., Chung, T.W.-H., Chu, M.-Y., Ng, Y.-Y., Lo, J., Chan, J., Tam, A.R., et al. (2020). Triple combination of interferon beta-1b, lopinavir-ritonavir, and ribavirin in the treatment of patients admitted to hospital with COVID-19: an open-label, randomised, phase 2 trial. Lancet *395*, 1695–1704.

Inoue, H., Matsuzaki, Y., Tanaka, A., Hosoi, K., Ichimura, K., Arasaki, K., Wakana, Y., Asano, K., Tanaka, M., Okuzaki, D., et al. (2015). γ-SNAP stimulates disassembly of endosomal SNARE complexes and regulates endocytic trafficking pathways. J. Cell Sci. *128*, 2781–2794.

Kozakov, D., Brenke, R., Comeau, S.R., and Vajda, S. (2006). PIPER: an FFT-based protein docking program with pairwise potentials. Proteins *65*, 392–406.

Kozakov, D., Hall, D.R., Xia, B., Porter, K.A., Padhorny, D., Yueh, C., Beglov, D., and Vajda, S. (2017). The ClusPro web server for protein-protein docking. Nat. Protoc. *12*, 255–278.

Kramer, M., Dutkowski, J., Yu, M., Bafna, V., and Ideker, T. (2014). Inferring gene ontologies from pairwise similarity data. Bioinformatics *30*, i34–i42.

Lamers, M.M., Beumer, J., van der Vaart, J., Knoops, K., Puschhof, J., Breugem, T.I., Ravelli, R.B.G., Paul van Schayck, J., Mykytyn, A.Z., Duimel, H.Q., et al. (2020). SARS-CoV-2 productively infects human gut enterocytes. Science *369*, 50–54.

Lokugamage, K.G., Hage, A., de Vries, M., Valero-Jimenez, A.M., Schindewolf, C., Dittmann, M., Rajsbaum, R., and Menachery, V.D. (2020). Type I Interferon Susceptibility Distinguishes SARS-CoV-2 from SARS-CoV. J. Virol. *94*, e01410-20.

Mar, K.B., Rinkenberger, N.R., Boys, I.N., Eitson, J.L., McDougal, M.B., Richardson, R.B., and Schoggins, J.W. (2018). LY6E mediates an evolutionarily conserved enhancement of virus infection by targeting a late entry step. Nat. Commun. *9*, 3603.

Mathew, D., Giles, J.R., Baxter, A.E., Oldridge, D.A., Greenplate, A.R., Wu, J.E., Alanio, C., Kuri-Cervantes, L., Pampena, M.B., D'Andrea, K., et al.; UPenn COVID Processing Unit (2020). Deep immune profiling of COVID-19 patients reveals distinct immunotypes with therapeutic implications. Science *369*, eabc8511.

Metz, P., Reuter, A., Bender, S., and Bartenschlager, R. (2013). Interferon-stimulated genes and their role in controlling hepatitis C virus. J. Hepatol. *59*, 1331–1341.

Miller, C.L. (2011). Stress Granules and Virus Replication. Future Virol. *6*, 1329–1338.

Mo, J., Chen, J., and Zhang, B. (2020). Critical roles of FAM134B in ER-phagy and diseases. Cell Death Dis. *11*, 983.

Monajemi, H., Fontijn, R.D., Pannekoek, H., and Horrevoets, A.J.G. (2002). The apolipoprotein L gene cluster has emerged recently in evolution and is expressed in human vascular tissue. Genomics *79*, 539–546.

Nanda, S.K., Johnson, R.F., Liu, Q., and Leibowitz, J.L. (2004). Mitochondrial HSP70, HSP40, and HSP60 bind to the 3′ untranslated region of the Murine hepatitis virus genome. Arch. Virol. *149*, 93–111.

Neil, S.J.D., Zang, T., and Bieniasz, P.D. (2008). Tetherin inhibits retrovirus release and is antagonized by HIV-1 Vpu. Nature *451*, 425–430.

Nguyen, N.T.H., Now, H., Kim, W.-J., Kim, N., and Yoo, J.-Y. (2016). Ubiquitin-like modifier FAT10 attenuates RIG-I mediated antiviral signaling by segregating activated RIG-I from its signaling platform. Sci. Rep. *6*, 23377.

Ostrowski, M., Carmo, N.B., Krumeich, S., Fanget, I., Raposo, G., Savina, A., Moita, C.F., Schauer, K., Hume, A.N., Freitas, R.P., et al. (2010). Rab27a and Rab27b control different steps of the exosome secretion pathway. Nat. Cell Biol. *12*, 19–30, 1–13.

Overmyer, K.A., Shishkova, E., Miller, I., Balnis, J., Bernstein, M.N., Peters-Clarke, T.M., Meyer, J.G., Quan, Q., Muehlbauer, L.K., Trujillo, E.A., et al. (2020). Large-scale Multi-omic Analysis of COVID-19 Severity. Cell Syst. *12*, 23–40.e7.

Page, N.M., Butlin, D.J., Lomthaisong, K., and Lowry, P.J. (2001). The human apolipoprotein L gene cluster: identification, classification, and sites of distribution. Genomics *74*, 71–78.

Pearce, M.M.P., Wormer, D.B., Wilkens, S., and Wojcikiewicz, R.J.H. (2009). An endoplasmic reticulum (ER) membrane complex composed of SPFH1 and SPFH2 mediates the ER-associated degradation of inositol 1,4,5-trisphosphate receptors. J. Biol. Chem. *284*, 10433–10445.

Pfaender, S., Mar, K.B., Michailidis, E., Kratzel, A., Boys, I.N., V'kovski, P., Fan, W., Kelly, J.N., Hirt, D., Ebert, N., et al. (2020). LY6E impairs coronavirus fusion and confers immune control of viral disease. Nat. Microbiol. *5*, 1330–1339.

Raudvere, U., Kolberg, L., Kuzmin, I., Arak, T., Adler, P., Peterson, H., and Vilo, J. (2019). g:Profiler: a web server for functional enrichment analysis and conversions of gene lists (2019 update). Nucleic Acids Res. *47* (W1), W191–W198.

Rayner, R.E., Makena, P., Prasad, G.L., and Cormet-Boyaka, E. (2019). Optimization of Normal Human Bronchial Epithelial (NHBE) Cell 3D Cultures for in vitro Lung Model Studies. Sci. Rep. *9*, 500.

Rodriguez-Frandsen, A., Martin-Sancho, L., Gounder, A.P., Chang, M.W., Liu, W.-C., De Jesus, P.D., von Recum-Knepper, J., Dutra, M.S., Huffmaster, N.J., Chavarria, M., et al. (2020). Viral determinants in H5N1 influenza A virus enable productive infection of HeLa cells. J. Virol. *94*, e0410.

Rosenzweig, R., Nillegoda, N.B., Mayer, M.P., and Bukau, B. (2019). The Hsp70 chaperone network. Nat. Rev. Mol. Cell Biol. *20*, 665–680.

Rusinova, I., Forster, S., Yu, S., Kannan, A., Masse, M., Cumming, H., Chapman, R., and Hertzog, P.J. (2013). Interferome v2.0: an updated database of annotated interferon-regulated genes. Nucleic Acids Res. *41*, D1040–D1046.

Schoggins, J.W., Wilson, S.J., Panis, M., Murphy, M.Y., Jones, C.T., Bieniasz, P., and Rice, C.M. (2011). A diverse range of gene products are effectors of the type I interferon antiviral response. Nature *472*, 481–485.

Schoggins, J.W., MacDuff, D.A., Imanaka, N., Gainey, M.D., Shrestha, B., Eitson, J.L., Mar, K.B., Richardson, R.B., Ratushny, A.V., Litvak, V., et al. (2014). Pan-viral specificity of IFN-induced genes reveals new roles for cGAS in innate immunity. Nature *505*, 691–695.

Seifert, L.L., Si, C., Saha, D., Sadic, M., de Vries, M., Ballentine, S., Briley, A., Wang, G., Valero-Jimenez, A.M., Mohamed, A., et al. (2019). The ETS transcription factor ELF1 regulates a broadly antiviral program distinct from the type I interferon response. PLoS Pathog. *15*, e1007634.

Seo, J.-Y., and Cresswell, P. (2013). Viperin regulates cellular lipid metabolism during human cytomegalovirus infection. PLoS Pathog. *9*, e1003497.

Shannon, P., Markiel, A., Ozier, O., Baliga, N.S., Wang, J.T., Ramage, D., Amin, N., Schwikowski, B., and Ideker, T. (2003). Cytoscape: a software environment for integrated models of biomolecular interaction networks. Genome Res. *13*, 2498–2504.

Singhal, A., Cao, S., Churas, C., Pratt, D., Fortunato, S., Zheng, F., and Ideker, T. (2020). Multiscale community detection in Cytoscape. PLoS Comput. Biol. *16*, e1008239.

Siu, Y.L., Teoh, K.T., Lo, J., Chan, C.M., Kien, F., Escriou, N., Tsao, S.W., Nicholls, J.M., Altmeyer, R., Peiris, J.S.M., et al. (2008). The M, E, and N structural proteins of the severe acute respiratory syndrome coronavirus are required for efficient assembly, trafficking, and release of virus-like particles. J. Virol. *82*, 11318–11330.

Spinnenhirn, V., Farhan, H., Basler, M., Aichem, A., Canaan, A., and Groettrup, M. (2014). The ubiquitin-like modifier FAT10 decorates autophagy-targeted Salmonella and contributes to Salmonella resistance in mice. J. Cell Sci. *127*, 4883–4893.

Sun, J., Ye, F., Wu, A., Yang, R., Pan, M., Sheng, J., Zhu, W., Mao, L., Wang, M., Huang, B., et al. (2020). Comparative transcriptome analysis reveals the intensive early-stage responses of host cells to SARS-CoV-2 infection. BioRxiv, 2020.04.30.071274.

Taylor, J.K., Coleman, C.M., Postel, S., Sisk, J.M., Bernbaum, J.G., Venkataraman, T., Sundberg, E.J., and Frieman, M.B. (2015). Severe Acute Respiratory Syndrome Coronavirus ORF7a Inhibits Bone Marrow Stromal Antigen 2 Virion Tethering through a Novel Mechanism of Glycosylation Interference. J. Virol. *89*, 11820–11833.

Tokarev, A., Suarez, M., Kwan, W., Fitzpatrick, K., Singh, R., and Guatelli, J. (2013). Stimulation of NF-κB activity by the HIV restriction factor BST2. J. Virol. *87*, 2046–2057.

Van Damme, N., Goff, D., Katsura, C., Jorgenson, R.L., Mitchell, R., Johnson, M.C., Stephens, E.B., and Guatelli, J. (2008). The interferon-induced protein BST-2 restricts HIV-1 release and is downregulated from the cell surface by the viral Vpu protein. Cell Host Microbe *3*, 245–252.

van der Made, C.I., Simons, A., Schuurs-Hoeijmakers, J., van den Heuvel, G., Mantere, T., Kersten, S., van Deuren, R.C., Steehouwer, M., van Reijmersdal, S.V., Jaeger, M., et al. (2020). Presence of Genetic Variants Among Young Men With Severe COVID-19. JAMA *24*, 1–11.

Wang, S.-M., Huang, K.-J., and Wang, C.-T. (2014). BST2/CD317 counteracts human coronavirus 229E productive infection by tethering virions at the cell surface. Virology *449*, 287–296.

Wang, S.M., Huang, K.J., and Wang, C.T. (2019). Severe acute respiratory syndrome coronavirus spike protein counteracts BST2-mediated restriction of virus-like particle release. J. Med. Virol. *91*, 1743–1750.

Whitt, M.A. (2010). Generation of VSV pseudotypes using recombinant ΔG-VSV for studies on virus entry, identification of entry inhibitors, and immune responses to vaccines. J. Virol. Methods *169*, 365–374.

Wilkinson, S. (2019). ER-phagy: shaping up and destressing the endoplasmic reticulum. FEBS J. *286*, 2645–2663.

Wilson, S.J., Schoggins, J.W., Zang, T., Kutluay, S.B., Jouvenet, N., Alim, M.A., Bitzegeio, J., Rice, C.M., and Bieniasz, P.D. (2012). Inhibition of HIV-1 particle assembly by 2′,3′-cyclic-nucleotide 3′-phosphodiesterase. Cell Host Microbe *12*, 585–597.

Wilson, G.J., Marakalala, M.J., Hoving, J.C., van Laarhoven, A., Drummond, R.A., Kerscher, B., Keeton, R., van de Vosse, E., Ottenhoff, T.H.M., Plantinga, T.S., et al. (2015). The C-type lectin receptor CLECSF8/CLEC4D is a key component of anti-mycobacterial immunity. Cell Host Microbe *17*, 252–259.

Yin, X., Riva, L., Pu, Y., Martin-Sancho, L., Kanamune, J., Yamamoto, Y., Sakai, K., Gotoh, S., Miorin, L., De Jesus, P.D., et al. (2021). MDA5 Governs the Innate Immune Response to SARS-CoV-2 in Lung Epithelial Cells. Cell Rep. *34*, 108628.

Yount, B., Curtis, K.M., Fritz, E.A., Hensley, L.E., Jahrling, P.B., Prentice, E., Denison, M.R., Geisbert, T.W., and Baric, R.S. (2003). Reverse genetics with a full-length infectious cDNA of severe acute respiratory syndrome coronavirus. Proc. Natl. Acad. Sci. USA *100*, 12995–13000.

Yu, M.K., Kramer, M., Dutkowski, J., Srivas, R., Licon, K., Kreisberg, J., Ng, C.T., Krogan, N., Sharan, R., and Ideker, T. (2016). Translation of Genotype to Phenotype by a Hierarchy of Cell Subsystems. Cell Syst. *2*, 77–88.

Zaderer, V., Hermann, M., Lass-Flörl, C., Posch, W., and Wilflingseder, D. (2019). Turning the World Upside-Down in Cellulose for Improved Culturing and Imaging of Respiratory Challenges within a Human 3D Model. Cells *8*, 1292.

Zang, R., Case, J.B., Castro, M.F.G., Liu, Z., Zeng, Q., Zhao, H., Son, J., Rothlauf, P.W., Hou, G., Bose, S., et al. (2020). Cholesterol 25-hydroxylase suppresses SARS-CoV-2 replication by blocking membrane fusion. BioRxiv, 2020.06.08.141077.

Zhang, T., Yin, C., Boyd, D.F., Quarato, G., Ingram, J.P., Shubina, M., Ragan, K.B., Ishizuka, T., Crawford, J.C., Tummers, B., et al. (2020). Influenza Virus Z-RNAs Induce ZBP1-Mediated Necroptosis. Cell *180*, 1115–1129.e13.

Zheng, F., Zhang, S., Churas, C., Pratt, D., Bahar, I., and Ideker, T. (2021). HiDeF: identifying persistent structures in multiscale ’omics data. Genome Biol. *22*, 21.

Zhu, C.-H., Kim, J., Shay, J.W., and Wright, W.E. (2008). SGNP: an essential Stress Granule/Nucleolar Protein potentially involved in 5.8s rRNA processing/transport. PLoS ONE *3*, e3716.

STAR★METHODS

KEY RESOURCES TABLE

REAGENT or RESOURCE	SOURCE	IDENTIFIER
Antibodies		
Rabbit anti-SARS-CoV-2 N	Gift from Kwok-Yung Yuen	N/A
mouse anti-HM1.24 (BST2)	Gift from Chugai Pharmaceutical Co., Kanagawa, Japan	N/A
mouse monoclonal anti-Orf7a	GeneTex	Cat# GTX632602; RRID:AB_2888320
rabbit polyclonal anti-BST2	NIH AIDS	Cat# 11721
mouse monoclonal anti-V5	Thermo Fisher Scientific	Cat# R960-25; RRID:AB_2556564
mouse monoclonal anti-GAPDH	GeneTex	Cat# GTX627408; RRID:AB_11174761
mouse monoclonal anti-FLAG M2	Sigma	Cat# F1804; RRID:AB_262044
rabbit monoclonal anti-β-actin	Cell Signaling	Cat# 4970; RRID:AB_2223172
rabbit monoclonal anti-CoxIV	Cell Signaling	Cat# 4850; RRID:AB_2085424
rat anti-FLAG-AlexaFluor-488	Biolegend	Cat# 637317; RRID:AB_2728470
mouse anti-HA-AlexaFluor-594	Biolegend	Cat# 901511; RRID:AB_2565073
donkey anti-mouse-AlexaFluor-488	Jackson ImmunoResearch	Cat# 715-545-150; RRID:AB_2340846
donkey anti-mouse-Rhodamine-Red-X	Jackson ImmunoResearch	Cat# 715-295-150; RRID:AB_2340831
Bacterial and virus strains		
SARS-CoV-2 USA-WA1/2020	BEI resources	Cat# NR-52281
SARS-CoV-1 icGFP	Yount et al., 2003	N/A
dOrf7a SARS-CoV-2	Gift from Ralph S. Baric, University of North Carolina at Chapel Hill; Hou et al., 2020	N/A
Chemicals, peptides, and recombinant proteins		
Universal type I IFN	R&D Systems	Cat# 11200-2
Fugene 6	Promega	Cat# E2691
Cas9	UC-Berkeley Macrolab	N/A
DAPI	KPL	Cat# 5930-0006
Lipofectamine RNAiMAX transfection reagent	Thermo Fisher	Cat# 13778150
Critical commercial assays		
GrowDex	UPM Biomedicals	N/A
Transwells	Corning	Cat# CLS3470
PneumaCult-ALI	StemCell	Cat# 05001
High-Capacity cDNA Reverse Transcription Kit	Thermo Fisher	Cat# 4368813
Power SYBR Green Master Mix	Thermo Fisher	Cat# 4368708
PneumaCult-Ex Plus Medium	StemCell	Cat# 05040
Deposited data		
RNA-seq data	GEO	GEO: GSE156295
Supplemental Items	Mendeley Data	https://doi.org/10.17632/743ty4chyz.2
Experimental models: Cell lines		
Vero E6	ATCC	Cat# CRL-1586; RRID:CVCL_0574
293T	ATCC	Cat# CRL-3216; RRID:CVCL_0063
HeLa	ATCC	Cat# CRL-1586; RRID:CVCL_0574
Calu-3	ATCC	Cat# HTB-55; RRID:CVCL_0609

(*Continued on next page*)

Continued

REAGENT or RESOURCE	SOURCE	IDENTIFIER
Huh7	Apath	Cat# LLC
BHK-21/WI-2	Kerafast	Cat# EH1011; RRID:CVCL_HB78
HeLa-ACE2	Gift from Thomas Rogers	N/A
293T-ACE2	This study	N/A
HeLa-ACE2 BST2 KO	This study	N/A
Experimental models: Organisms/strains		
HTBE (RNAseq)	ATCC	Cat# PCS-300-010
HTBE (infection studies)	Lonza	Cat# CC2540S
Oligonucleotides		
ISG54 primer	IDT	Fwd: CAG CTG AGA ATT GCA CTG CAA Rev: GTA GGC TGC TCT CCA AGG AA
TBP primer	IDT	Fwd: CCA CTC ACA GAC TCT CAC AAC Rev: CTG CGG TAC AAT CCC AGA ACT
ActinB CTRL Mix primer	Applied Biosystems	4352341E
SARS-CoV-2 N primer	Applied Biosystems	Fwd: TTACAAACATTGGCCGCAAA Rev: GCGCGACATTCCGAAGAA
scrambled siRNA	Ambion	AATCGATCATAGGACGAACGC
IRF9 siRNA	Ambion	CAACAAGAGTTCTGAATTTAA
BST2 siRNA	Ambion	Cat# AM16708 - 14490
BST2 gRNA	Dharmacon	Cat# CM-011817-01 to CM-011817-05
Non-targeting negative control gRNA	Dharmacon	Cat# U-007501
Recombinant DNA		
pLX304 V5-tagged human ORFs	ORFeome library	http://horfdb.dfci.harvard.edu
psPAX2	Addgene	Cat# 12260; RRID:Addgene_12260
pMD2.G	Addgene	Cat# 12259; RRID:Addgene_12259
pCG1-COV2-S-HA	Gift from Prof. Stefan Pohlmann; Hoffmann et al., 2020	N/A
SARS-CoV-2 expression vectors	This study	N/A
Software and algorithms		
Prism 8	Graphpad	https://www.graphpad.com/scientific-software/prism/
Slidebook software V.6	Imaging Innovations, Inc	N/A
ClusPro	Kozakov et al., 2017	N/A
Cytoscape v3.8.0	N/A	https://cytoscape.org
CDAPS	Singhal et al., 2020; Zheng et al., 2021	https://apps.cytoscape.org//apps/cycommunitydetection
Interferome	Rusinova et al., 2013	N/A

RESOURCE AVAILABILITY

Lead contact

Further information and requests for resources and reagents should be directed to and will be fulfilled by the lead contact, Sumit K. Chanda (*schanda@sbpdiscovery.org*).

Materials availability

Stable cell lines and expression constructs generated for this study can be obtained upon request from the lead contact. Commercially available reagents are indicated in the key resources table.

Data and code availability

The accession number for the A549 and HTBE RNA-seq data reported in this paper is GEO: GSE156295. In addition, original data have been deposited to Mendeley Data: https://doi.org/10.17632/743ty4chyz.2

EXPERIMENTAL MODEL AND SUBJECT DETAILS

Viruses, cell lines, and primary cultures

SARS-CoV-2 USA-WA1/2020, isolated from an oropharyngeal swab from a patient with a respiratory illness who developed clinical disease (COVID-19) in January 2020 in Washington, USA, was obtained from BEI Resources (NR-52281). SARS-CoV-1 icGFP has been previously described (Yount et al., 2003). The recombinant dOrf7a SARS-CoV-2 was kindly provided by Ralph Baric (Hou et al., 2020). These viruses were propagated using Vero E6 cells and stored at −80°C. Plaque forming unit (PFU) assays were performed to titrate the cultured virus. All experiments involving live SARS-CoV-2 followed the approved standard operating procedures of the Biosafety Level 3 facility at the Sanford Burnham Prebys Medical Discovery Institute. All work with SARS-CoV-1 was performed in a Biosafety Level 3 laboratory and approved by the University of Maryland Institutional Biosafety Committee.

Vero E6 (ATCC CRL-1586), 293T (ATCC CRL-3216), HeLa (ATCC CRL-1586), Calu-3 (ATCC HTB-55), and Huh7 (Apath LLC, Brooklyn) cells were maintained in cell growth media: Dulbecco's modified eagle medium (DMEM, GIBCO) supplemented with 10% heat-inactivated fetal bovine serum (FBS, GIBCO), 50 U/mL penicillin - 50 μg/mL streptomycin (Fisher Scientific), 1 mM sodium pyruvate (GIBCO), 10 mM 4-(2-hydroxyethyl)-1-piperazineethanesulfonic acid (HEPES, GIBCO), and 1X MEM non-essential amino acids solution (GIBCO). BHK-21/WI-2 cells (Kerafast, MA) were maintained in DMEM (GIBCO) supplemented with 10% heat-inactivated FBS (GIBCO) and 50 U/mL penicillin - 50 μg/mL streptomycin. For the SARS-CoV-1 experiments, Vero E6 cells were cultured in DMEM (Quality Biological), supplemented with 10% (v/v) fetal bovine serum (FBS; GIBCO), 1% (v/v) penicillin/streptomycin (pen/strep, 10,000 U/ml / 10 mg/ml; Gemini Bio-Products) and 1% (v/v) L-glutamine (GIBCO), and 293T-ACE2 cells were cultured in DMEM supplemented with 10% FBS and 1% pen/strep. Cells were maintained at 37°C and 5% CO2. Human tracheobronchial epithelial (HTBE) cells (ATCC PCS-300-010) for the RNAseq experiment were cultured in commercially available airway epithelial cell basal medium following manufacturer's protocol (ATCC). HTBE cells were derived from one donor and all tissues used for isolation of these cells were obtained under informed consent and conform to HIPAA standards to protect the privacy of the donors' personal health information. For the ISG overexpression experiment, HTBE cells from a single donor (Lonza CC2540S) were expanded in PneumaCult Ex Plus medium and differentiated in PneumaCult ALI medium (Stemcell 05040, 05001). 293T and HeLa cells stably expressing ACE2 (293T-ACE2/HeLa-ACE2) were generated by transducing HEK293T or HeLa cells with human ACE2-expressing lentiviruses, followed by selection of resistant cells with puromycin (InvivoGen) at 2 μg/ml for 14 days. The resistant cells were then maintained in cell growth media supplemented with 1 μg/ml puromycin. ACE2 expression was confirmed by western blot analysis. All cells were tested and were confirmed to be free of mycoplasma contamination.

METHOD DETAILS

Antibodies

The antibodies used in this study include: *Immunofluorescence:* rabbit-anti-SARS-CoV-2 N antibody (gift from Kwok-Yung Yuen, University of Hong Kong), mouse anti-HM1.24 (BST2) (a gift from Chugai Pharmaceutical Co., Kanagawa, Japan), rat anti-FLAG-AlexaFluor-488 (Biolegend, #637317), mouse anti-HA-AlexaFluor-594 (Biolegend, #901511), donkey anti-mouse-AlexaFluor-488 (Jackson ImmunoResearch, #715-545-150), donkey anti-mouse-Rhodamine-Red-X (Jackson ImmunoResearch, #715-295-150), and mouse anti-V5 tag (Invitrogen, R960-25). Western *blotting:* mouse monoclonal anti-Orf7a (GeneTex #GTX632602), rabbit polyclonal anti-BST2 (NIH AIDS Reagent Program, Division of AIDS, NIAID, NIH: Anti-BST-2 Polyclonal (cat #11721) from Drs. Klaus Strebel and Amy Andrew), mouse monoclonal anti-V5 tag (Invitrogen, #R960-25), mouse monoclonal anti-GAPDH (GeneTex, #GTX627408), mouse monoclonal anti-FLAG M2 (Sigma, #F1804), rabbit monoclonal anti-β-actin antibody (Cell Signaling, #4970) and rabbit monoclonal anti-CoxIV antibody (Cell Signaling #4850).

Plasmids

Lentiviral constructs: pLX304 V5-tagged human ORFs constructs for each of the ISGs, and GFP and CAT negative controls were obtained from the ORFeome library. psPAX2 (Addgene, #12260), and pMD2.G (Addgene, #12259). *SARS-CoV-2 constructs:* dsDNA gene fragments (gBlocks) encoding human-codon-optimized SARS-CoV-2 proteins M, M-FLAG, E, E-V5, N, N-V5, and Orf7a N- or C-terminally tagged with 3xFLAG tag, corresponding to the SARS-CoV-2 Wuhan-Hu-1 isolate (GenBank MN908947.3), were synthesized by Integrated DNA Technologies (IDT). The gene fragments were inserted into the pcDNA3.1(-) backbone between NotI and EcoRI restriction sites using an In-fusion seamless cloning strategy (Takara Bio). The mammalian expression vector encoding COV2 S, pCG1-COV2-S-HA, was obtained from Prof. Stefan Pohlmann (Infection Biology Unit, German Primate Center - Leibniz Institute for Primate Research, University Göttingen; Hoffmann et al., 2020).

Primers

Primers used for this study include *ISG54* Forward: 5′ CAG CTG AGA ATT GCA CTG CAA 3′, *ISG54* Reverse: 5′ GTA GGC TGC TCT CCA AGG AA 3′, *TBP* Forward: 5′ CCA CTC ACA GAC TCT CAC AAC 3′, and *TBP* Reverse: 5′ CTG CGG TAC AAT CCC AGA ACT 3′.

RNA-seq experiments

HTBE and A549 cells were seeded overnight and then treated with 100 IU/ml universal type I interferon (IFN, R&D Systems), or left untreated. At 8 h post-treatment, cell were lysed in Trizol (Thermo Fisher) and RNA was extracted using RNeasy Mini Kit (QIAGEN). Strand-specific ribosomal RNA-depleted sequencing libraries were produced according to standard Illumina protocols, and sequencing was carried out on an Illumina HiSeq 2500. The human hg38 reference genome and RefSeq gene annotation were used for spliced read alignment and gene assignment. Experiments were conducted in duplicate and 412 genes were defined as ISGs based on average log2FC > 1.5 and p value < 0.05.

Overexpression cDNA screen

A targeted overexpression cDNA screen was carried out in human epithelial cells to identify ISGs that restrict the replication of SARS-CoV-2. 399 ISGs were selected for this gain-of-function screen based on experimental RNA-seq data (*see* Figure S1A), published data (*see* Figure S1B), and availability as full-length, sequence-validated cDNA clones. These cDNAs were hand-picked from the ORFeome collection, which contains ~17,000 full-length, sequenced, V5-epitope tagged human ORFs in the lentiviral expression vector pLX304. Each of these 399 cDNAs were individually arrayed in 384-well plates at a concentration of 40ng/well along with human ACE2 and TMPRSS2 (10 ng), and 0.25 μL of the transfection reagent Fugene 6 (Promega, #E2691). After 20 min incubation at room temperature, 3,000 293T cells diluted in cell growth media (see *cells and viruses* section) were seeded per well and incubated at 37°C, 5% CO_2. At 30 h post-transfection, cells were mock-treated or infected with SARS-CoV-2 (USA-WA1/2020) at a MOI 0.0625 for 40 h at 37°C, 5% CO_2. Cells were then fixed with 5% PFA (Boston BioProducts) for 4 hours at room temperature and then washed twice with 1xPBS. Cells were permeabilized with 0.5% Triton X-100 for 20 min, followed by two washes with 1xPBS and blocking with 3% BSA (Sigma) for 1 h at room temperature. Anti-SARS-CoV-2 N rabbit serum was added for 1 h at room temperature, followed by three washes with 1xPBS and a 1-h incubation with Alexa Fluor 568-conjugated anti-rabbit secondary antibody (Thermo Fisher Scientific) diluted in 3% BSA. Following three washes with PBS, cells were stained with DAPI (4,6-diamidine-2-phenylindole, KPL), and plates were sealed and stored at 4°C until imaging.

High-content imaging and data analysis

Viral replication was assessed using high-throughput microscopy. The assay plates were imaged using the IC200 imaging system (Vala Sciences) located at the Conrad Prebys Center for Chemical Genomics (CPCCG). The analysis software Columbus v2.5 (Perkin Elmer) was used to calculate % infection (number Alexa 568+ objects/number DAPI+ objects). Screens were run in duplicate and the % infection values for each well were normalized to the median of the negative control CAT, and used to calculate the log2FC. The hit calling strategy was based on log2FC. Factors with a corresponding log2FC < 4 x the standard deviation (SD) of CAT log2FC, and cell number > 70% of CAT were considered restriction factors.

Interferon treatment

293T cells that were transfected with human ACE2 and TMPRSS2 (10 ng) for 30 h were then mock-treated or treated with increasing doses of universal type I interferon (IFN, R&D Systems, #11200-2). After 6 h of incubation at 37°C, 5% CO_2, cells were infected with SARS-CoV-2 (MOI 0.0625) for 40 h at 37°C, 5% CO_2. Cells were then fixed and subjected to DAPI staining and anti-SARS-CoV-2 N rabbit serum staining to determine % of infected cells.

Generation of lentiviruses

Lentiviruses were generated for each of the 65 ISGs that were found to restrict SARS-CoV-2 replication. Briefly, 293T cells at passage 10 were cultured in monolayer on matrigel-coated plates. After reaching 90% of density, three plasmids, including pLX304-ISG/GFP, psPAX2 (Addgene), and pMD2.G (Addgene), were co-transfected into cells at a ratio of 3:2:1 using PEI (VWR). After 16 h incubation, transfection media were replaced with fresh DMEM supplemented with 10% FBS. Viral supernatants were collected at 48 h post-transfection with an estimated transduction unit of $2x10^4$ lentiviral particles.

Generation of the 293T-ACE2-ISG/GFP and Calu-3-ISG/GFP cells

Lentiviruses were used to transduce 293T-ACE2 or Calu-3 cells (MOI = 3) pre-treated with 10 μg/ml Polybrene (Life Technologies), followed by selection of resistant cells with Blasticidin (InvivoGen) at 10 μg/ml (293T-ACE2) and 8 μg/ml (Calu-3) for 14 days. 293T-ACE2-ISG/GFP and Calu-3-ISG/GFP resistant cells were maintained in cell growth media supplemented with 2 μg/ml Blasticidin.

Generation and infection of HTBE cells stably expressing GFP/ISG

Cells generation. HTBE cells at passage 2 were trypsinized and resuspended in a mixture of expansion medium (Stemcell 05040), 0.5% GrowDex® (UPM Biomedicals), and 4 μg/mL polybrene. ISG/GFP lentiviruses generated following the described protocol (*see* Generation of lentiviruses) were added at MOI = 2, and the suspension was then seeded in permeable supports (Corning CLS3470). After allowing cells to attach to the support overnight, excess GrowDex® mix was removed. Upon confluence, apical medium was removed to establish an air-liquid interface and basal medium was switched to PneumaCult ALI (Stemcell 05001). Cultures differentiated at air-liquid interface for 30 days before infection. Medium was supplemented with 2 μg/ml Blasticidin from 48 hours post transduction. Transduction efficiency of these cultures was determined based on GFP imaging of the GFP-transduced cells (average GFP^+ cells = 74.46%).

SARS-CoV-2 infection studies. HTBE cells stably expressing the indicating ISGs, or negative control GFP, were washed twice with warm PBS prior to viral infection. Subsequently, 1x106 pfu SARS-CoV-2 per well diluted in PBS (equivalent to MOI = 1) were added to the apical side of each cell chamber. After 1 h incubation at room temperature, the viral inoculum was removed, cells were washed twice with warm PBS, and 150 μL PBS were added to the apical side. At 18 h post-infection, supernatants were collected, and the amount of SARS-CoV-2 focus forming units per ml (FFU/ml) analyzed using Vero E6 cells.

Network analyses

Rationale. To understand the biochemical and functional context by which the identified antiviral ISGs function, we built a model that places these hits in the context of known protein-protein interactions. Each cluster of interacting proteins are then organized in a hierarchy where larger clusters are composed of smaller ones (Kramer et al., 2014; Yu et al., 2016). Unlike the human-curated Gene Ontology (GO), the structure is derived by the use of a multi-scale clustering algorithm applied to a reference protein-protein interaction network, in this case, a high-confidence subset of the STRING database. To focus the model on the experimental data, it is built using the ISGs found to inhibit SARS-CoV-2 replication in this study (the ‘‘hits’’) and their close neighbors. The interpretation of the experiment is performed by projecting the hits onto the clusters in the model, analogous to mapping them to GO terms (Dutkowski et al., 2013). Candidate names are proposed for each cluster by performing functional enrichment, finding the closest matching pathways and GO terms. Comparing this model to the result of a GO analysis, it has the advantages that its terms (clusters) are algorithmically derived from protein interactions that are in a sense ‘‘proximal’’ to the hits so that the hits can be then investigated in the context of their underlying interactions.

Approach. To explore the highest confidence interactions of ‘‘hit’’ proteins, we selected the STRING - Human Protein Links - High Confidence (Score > = 0.7) protein-protein interaction network available on NDEx as the ‘‘background’’ network (link provided below). We then performed network propagation to select a neighborhood of 343 proteins ranked highest by the algorithm with respect to these seeds (Carlin et al., 2017). This ‘‘neighborhood’’ network (including all edges among the 343 proteins) was extracted from the background network. We then identified densely interconnected regions, i.e., ‘‘communities’’ within the neighborhood network, using the community detection algorithm HiDeF via the Community Detection APplication and Service (CDAPS) (Singhal et al., 2020; Zheng et al., 2021) (app available at http://apps.cytoscape.org/apps/cycommunitydetection). The result of HiDeF from CDAPS was a ‘‘hierarchy’’ network where each node represented a community of proteins, and edges denoted containment of one community (the ‘‘child’’) by another (the ‘‘parent’’). Finally, the hierarchy network was styled, communities were labeled by functional enrichment using gProfiler (via CDAPS), p values were calculated based on the accumulative hypergeometric distribution, and a layout was applied. The STRING - Human Protein Links - High Confidence (Score > = 0.7) network is available in the Network Data Exchange (NDEx) at http://ndexbio.org/#/network/275bd84e-3d18-11e8-a935-0ac135e8bacf.

Evaluation of factors in network with ISGs

The 44 factors found to be associated with the identified antiviral ISGs (displayed in Figures 2B–2E), were evaluated for their responsiveness to IFN and SARS-CoV-2 infection, as well as their expression in relevant cell types. These factors were therefore cross-compared with RNAseq datasets of IFN-treated A549 and HTBE cells conducted within this study, as well as a public database of IFN stimulated genes (Interferome) (Rusinova et al., 2013). In addition, factors were cross-referenced with RNAseq datasets of 293T and A549 cells (Rodriguez-Frandsen et al., 2020), single cell RNAseq data of human lung cells (Deprez et al., 2020), and published RNAseq datasets of various cell types infected with SARS-CoV-2 (Blanco-Melo et al., 2020; Emanuel et al., 2020; Sun et al., 2020). Data are shown in Table S4.

Generation of pseudotyped SARS-CoV-2 virus

VSV pseudotyped with spike (S) protein of SARS-CoV-2 was generated according to a published protocol (Whitt, 2010). Briefly, BHK-21/WI-2 cells (Kerafast, MA) transfected with SARS-CoV-2 S protein were inoculated with VSV-G pseudotyped ΔG-luciferase VSV (Kerafast, MA). After a 2 hour incubation at 37°C, the inoculum was removed and cells were treated with DMEM supplemented with 5% FBS, 50 U/mL penicillin, and 50 μg/mL streptomycin. Pseudotyped particles were collected 24 h post-inoculation, then centrifuged at 1,320 × g to remove cell debris and stored at −80°C until use.

Mapping into SARS-CoV-2 infectious cycle studies

Mapping studies were conducted in parallel using 293T-ACE2-ISG/GFP cells. Briefly, multiple 96-well plates were seeded with 50,000 293T-ACE2-ISG/GFP cells/well and incubated overnight at 37°C, 5% CO_2. To determine the effect of the identified ISGs on *viral entry*, 293T-ACE2-ISG/GFP cells were infected with VSV-S-luciferase or VSV-G-luciferase and incubated for 16 h. The activity of firefly luciferase was then measured using the bright-Glo luciferase assay (Promega) for quantitative determination. To measure *RNA replication* and *late stages*, cells were infected with SARS-CoV-2 (USA-WA1/2020) at a MOI 4 for 1 h on ice. Viral inoculum was removed and cells were washed twice with 1xPBS and supplemented with cell growth media (see cells and viruses section). At 6 h post-infection, SARS-CoV-2 *RNA replication* was measured. Briefly, intracellular viral RNA was purified from infected cells using the TurboCapture mRNA Kit (QIAGEN) in accordance with the manufacturer’s instructions. The purified RNA was subjected to first-strand cDNA synthesis using the high-capacity cDNA reverse transcription kit (Applied Biosystems, Inc). Real-time quantitative PCR (RT-qPCR) analysis was then performed using TaqPath one-step RT-qPCR Master Mix (Applied Biosystems, Inc) and, ActinB

CTRL Mix (Applied Biosystems, Inc) for housekeeping genes, and the following primers and probe for qPCR measurements of viral genes: N-Fwd: 5′-TTACAAACATTGGCCGCAAA-3′; N-Rev: 5′-GCGCGACATTCCGAAGAA-3′; N-Probe: 5′-FAM-ACAATTTGCCCCCAGCGCTTCAG-BHQ-3′. To evaluate *late stages*, supernatants collected at 18 h post-infection were used to infect naive Vero E6 cells. At 18 h post-infection cells were then fixed with 5% PFA (Boston BioProducts) for 4 hours at room temperature and then subjected to immunostaining and imaging for SARS-CoV-2 N protein and DAPI (described in Overexpression cDNA screen section).

Generation of the integrated model of SARS-CoV-2 cellular restriction mechanisms

ISGs that were found to inhibit SARS-CoV-2 replication in this study were evaluated for pathway enrichment using the following ontology sources: KEGG Pathway, gene ontology (GO) biological processes, Reactome Gene Sets, Canonical Pathways, CORUM, TRRUST, DisGeNET, PaGenBase. These data were reviewed and refined manually using published literature so factors were clustered into functional categories that are shown in light blue boxes and labeled accordingly. These clusters were then placed at the position likely to be affecting viral replication using SARS-CoV-2 life cycle as reference and the experimental data generated in Figure 3. SARS-CoV-2 protein interactors are shown in yellow (Gordon et al., 2020). Dotted lines denote virus-host protein interactions.

Generation of CRISPR-Cas9 BST2 KO HeLa-ACE2 cells

Detailed protocols for RNP production have been previously published (Hultquist et al., 2019). Briefly, lyophilized guide RNA (gRNA) and tracrRNA (Dharmacon) were suspended at a concentration of 160 μM in 10 mM Tris-HCL, 150 mM KCl, pH 7.4. 5 μL of 160 μM gRNA was mixed with 5 μL of 160 μM tracrRNA and incubated for 30 min at 37°C. The gRNA:tracrRNA complexes were then mixed gently with 10 μL of 40 μM Cas9 (UC-Berkeley Macrolab) to form CRISPR-Cas9 ribonucleoproteins (crRNPs). Five 3.5 μL aliquots were frozen in Lo-Bind 96-well V-bottom plates (E&K Scientific) at −80°C until use. BST2 gene was targeted by 5 pooled gRNA derived from the Dharmacon pre-designed Edit-R library for gene knock-out. *BST2* (g1:TGCATCCAGGGAAGCCATTA, CM-011817-01; g2:TTGGGCCTTCTCTGCATCCA, CM-011817-02; g3:TTGAGGAGCTTACCACAGTG, CM-011817-03; g4: TCACTGCCCGAAGGCCGTCC, CM-011817-04; g5: CACCATCAAGGCCAACAGCG, CM-011817-05). Non-targeting negative control gRNA (Dharmacon, U-007501) was delivered in parallel. Each electroporation reaction consisted of 2.5x10^5 HeLa-ACE2 cells, 3.5 μL crRNPs, and 20 μL electroporation buffer. HeLa-ACE2 cells were grown in fully supplemented MEM (10% FBS, 1xPen/Strep, 1x non-essential amino acids) to 70% confluency, suspended and counted. crRNPs were thawed and allowed to come to room-temperature. Immediately prior to electroporation, cells were centrifuged at 400 x g for 3 minutes, supernatant was removed by aspiration, and the pellet was resuspended in 20 μL of room-temperature SE electroporation buffer plus supplement (Lonza) per reaction. 20 μL of cell suspension was then gently mixed with each crRNP and aliquoted into a 96-well electroporation cuvette for nucleofection with the 4-D Nucleofector X-Unit (Lonza) using pulse code EO-120. Immediately after electroporation, 80 μL of pre-warmed media was added to each well and cells were allowed to rest for 30 minutes in a 37°C cell culture incubator. Cells were subsequently moved to 12-well flat-bottomed culture plates pre-filled with 500 μL pre-warmed media. Cells were cultured at 37°C / 5% CO2 in a dark, humidified cell culture incubator for 4 days to allow for gene knock-out and protein clearance prior to downstream applications.

siRNA transfection in Calu-3 cells

Transfections were carried out in 24-well plates: 0.6 μL siRNA (at 20nM) was diluted in 149.4 μL of Optimem and mixed with 1 μL Lipofectamine RNAiMAX transfection reagent diluted in 149 μL Opti-MEM media (both reagents Thermo Fisher Scientific). After an incubation period of 20 min at room temperature to enable the formation of siRNA-transfection reagent complexes, Calu-3 cells were then seeded on top of the complexes and incubated for 48 h at 37°C, 5% CO_2. Cells were then mock-treated or treated with 18 IU/ml universal type I interferon (IFN, R&D Systems) for 6 h at 37°C, 5% CO_2 and then infected with SARS-COV-2 (MOI 0.75). After a 1-h incubation at room temperature, the inoculum was removed and replaced with 300 μL of fresh cell media and cells were incubated at 37°C, 5% CO_2. At indicated time points, supernatants were collected and subjected to SARS-CoV-2 viral growth assays. All siRNAs are from Ambion. Target sequences custom siRNAs: scrambled siRNA (5′-AATCGATCATAGGACGAACGC-3′), and IRF9 siRNA (5′-CAACAAGAGTTCTGAATTTAA-3′). BST2 siRNA (AM16708 #14490).

SARS-CoV-2 viral growth assays

To evaluate SARS-CoV-2 viral growth, the amount of released infectious particles was measured by plaque assay. Briefly, supernatants from SARS-CoV-2 infected cells were collected at indicated time points and stored at −80°C until used. 600,000 Vero E6 cells were seeded and incubated overnight at 37°C / 5% CO2 in 12-well plates. Confluent Vero E6 cells were then washed once with 1xPBS and infected with 100 μl of virus-containing supernatants that were serially diluted 1:10. Plates were incubated 1 h at room temperature, followed by inoculum removal and addition of 1ml overlay media (2xMEM and 2.5% Avicel (FMC BioPolymer, RC-591 NF) at 1:1 ratio). 2xMEM contains 100 mL 10x MEM (GIBCO), 10 mL 100x penicillin-streptomycin (Fisher Scientific), 10 mL 100x L-Glutamine, 6 mL 35% BSA, 10 mL 10 mM 4-(2-hydroxyethyl)-1-piperazineethanesulfonic acid (HEPES, GIBCO), 24 mL 5% NaHCO3 (GIBCO) and 340 mL water. Plates were incubated 3 days at 37°C, 5% CO_2, and then fixed and stained using 0.1% Crystal Violet and 5% PFA (Boston BioProducts) overnight at 4°C.

VLP assays

293T cells seeded in 6-well plates were transfected using Lipofectamine 2000 (Thermo-Fisher) with 625 ng each of plasmids encoding M-FLAG, E-V5, N-V5 (Figure 5E), or 500 ng of M, E, and N-V5 (Figure S3E), with or without 625 ng 3xFLAG-Orf7a or human codon-optimized HIV-1 Vpu (pVpHu from Klaus Strebel) with or without 75 ng BST2 (pcDNA3.1-BST-2 from Autumn Ruiz and Edward Stephens). After 24 hours, supernatants were collected and clarified of cell debris then pelleted through 20% sucrose at 23,500 x g for 1 hr at 4°C. Pelleted VLPs and cells were lysed in 2X Laemmli SDS-PAGE buffer, then run on 12% SDS-PAGE gels, transferred to PVDF membranes and blotted with the indicated antibodies.

Colocalization studies

Immunofluoresce staining. 1×10^5 HeLa-ACE2 cells were seeded on 12 mm glass coverslips in 24-well plates, 24 h prior to transfection. The cells were transfected with 800 ng total plasmid DNA, using Lipofectamine 2000 (Invitrogen), diluted in Optimem, according to manufacturer's instructions. HeLa-ACE2 cells were either transfected with equal amounts (200 ng) of SARS-CoV-2 structural proteins M, E, N, S-HA, or M-FLAG, E, N, and empty plasmid (pcDNA3.1). HeLa-ACE2 cells were also transfected with 800 ng Orf7a-3xFLAG. 24 h post-transfection, cells were washed briefly in 4°C PBS before incubation with ice-cold 4% paraformaldehyde (PFA, diluted in PBS, pH 7.4). The PFA was allowed to warm to RT as the cells were fixed for 20 minutes, the PFA was removed and cells washed 3x in 1XPBS (5 min per wash). The fixed cells were quenched with 50 mM Ammonium chloride (in PBS) for 5 minutes RT, washed 3 x in PBS, and permeabilized with 0.2% Triton X-100 for 7 minutes RT. The cells were washed before incubation with 2% bovine serum albumin (BSA) in PBS for 30 minutes, prior to incubation with primary antibodies overnight at 4°C. Cells transfected with M, E, N and S-HA were stained overnight with mouse anti-HM1.24 (BST-2) antibody (diluted 1:300 in 1% BSA in PBS) at 4°C. The following day, the cells were washed 3x PBS and incubated with donkey anti-mouse-AlexaFluor-488 (1:400) for 2hr RT. The cells were washed 3x PBS (10 min per wash) and blocked with 2% BSA in PBS supplemented with 5% normal mouse serum for 1 hr RT, briefly washed in 2% BSA, and incubated with mouse anti-HA-Alexa-594 (1:200) and 4′,6-diamidino-2-phenylindole (DAPI), diluted to 1 μg/ml for 2 hr RT. Cells transfected with M-FLAG, E and N were stained overnight with mouse anti-BST-2 (diluted 1:300 in 1% BSA in PBS). The following day the cells were washed 3x PBS and incubated with donkey anti-mouse-Rhodamine-Red-X (1:400) for 2 hr RT. The cells were washed 3x PBS (10 min per wash) and blocked with 2% BSA in PBS supplemented with 5% normal mouse serum for 1 hr RT, briefly washed in 2% BSA, and incubated with rat anti-FLAG-Alexa 488 (diluted 1:200) and 1 μg/ml DAPI for 2 hr RT. Cells transfected with Orf7a-3xFLAG were stained overnight with mouse anti- HM1.24 (diluted 1:300). The following day the cells were washed 3x PBS and incubated with donkey anti-mouse-Rhodamine-Red-X (1:400) for 2 hr RT. The cells were washed 3x PBS (10 min per wash) and blocked with 2% BSA in PBS supplemented with 5% normal mouse serum for 1 hr RT, briefly washed in 2% BSA, and incubated with rat anti-FLAG-Alexa 488 (diluted 1:200) and 1 μg/ml DAPI for 2 hr RT. Following immunostaining, the cells were washed extensively in PBS, and briefly in distilled-water, before mounting in Mowiol (Polyvinyl alcohol) mounting medium (prepared in-house).

Microscopy. Images were captured at 100x magnification (1344 × 1024 pixels) using an Olympus IX81 widefield microscope fitted with a Hamamatsu CCD camera. For each field, a Z series of images was collected, deconvolved using the nearest-neighbor algorithm (Slidebook software V.6, Imaging Innovations, Inc) and presented as Z stack projections. Inset images are deconvolved single z section images. Arrow heads indicate areas of colocalization, scale bar = 10 μm. Image brightness was adjusted using Adobe Photoshop CS3.

Evaluation of surface BST2 levels

293T cells in 6-well plates were transfected with 625 ng each of plasmids encoding M, E and N, 400 ng of GFP-encoding plasmid pcgGFP as a transfection control and 75 ng pcBST2-WT with or without 625 ng Orf7a-FLAG or HIV-1 Vpu. After 36 hours, cells from duplicate wells were harvested, stained for surface BST2 with Alexa Fluor 647-conjugated mouse anti-BST2 antibody (Biolegend, RS38E), fixed, and analyzed for GFP and surface BST2 expression by flow cytometry.

In silico docking of Orf7a and BST2 ectodomain by ClusPro

Based on the structures of BST2 (3MQC) and Orf7a (1XAK), we explored the potential interaction mechanism by recently developed protein docking tool ClusPro (Kozakov et al., 2017). ClusPro utilizes a comprehensive docking method, which combines rigid-body docking by the Fast Fourier Transform-based PIPER algorithm (Kozakov et al., 2006), RMSD-based clustering to find largest clusters representing the most likely models, and refinement using energy minimization by CHARMM (Brooks et al., 2009). The docking between Orf7a and the BST2 dimer generated a very clear solution, where the top 2 hits (related by a 2-fold symmetry) have cluster sizes (237 and 220) significantly larger than the rest (all < 60), thus suggesting a most likely binding mode.

Orf7a co-immunoprecipitation studies

293T cells were seeded in 6-well plates and then transfected with 1 μg of BST2 expression plasmid (WT or the N2Q mutant, both plasmids previously described at (Tokarev et al., 2013)) and 3 μg either empty plasmid, Orf7a-FLAG or HIV-1 Vpu-FLAG expression plasmid. After 24 hours, the cells were harvested, lysed, then immunoprecipitated using anti-FLAG M2 magnetic beads (Sigma), and eluted with 2X Laemmli SDS-PAGE buffer. Cell lysates and FLAG IP were run on 12% SDS-PAGE gels, transferred to PVDF membranes, and blotted with mouse anti-GAPDH, rabbit anti-BST2 and mouse anti-FLAG antibodies.

SARS-CoV-1 infection

293T-ACE2 cells stably expressing indicated ISGs were cultured to reach ∼70%–80% confluency in 96-well plates. Cells were infected at MOI 0.01 for 48 hours at which time supernatant was collected. Infectious virus release from the cells was calculated by median tissue culture infectious dose (TCID50) assay using Vero E6 cells.

Virus names and abbreviations

Chikungunya virus (CHIKV), O’nyong’nyong virus (ONNV), Sindbis virus (SINV), Venezuelan equine encephalitis virus (VEEV), Yellow fever virus (YFV), Human parainfluenza virus type 3 (PIV3), Human metapneumovirus (HMPV), Newcastle disease virus (NDV), Respiratory syncytial virus (RSV), Measles virus (MV), Equine viral arteritis (EVA), Bunyamwera virus (BUNV), poliovirus (PV), coxsackievirus (CBV), vaccinia virus (VV).

QUANTIFICATION AND STATISTICAL ANALYSIS

Statistical parameters including the exact value of n, dispersion and precision measures (mean ± SD or SEM), and statistical significance are reported in the figures and figure legends. Statistical significance between groups was determined using GraphPad Prism 8.0 (GraphPad, San Diego, CA), and the test used is indicated in the figure legends.